

From Frequency Bias to Spectral Balance: Operator-Aware Preconditioners for PINNs

Roy Y. He ^{*} Ying Liang [†] Hongkai Zhao [‡] Yimin Zhong [§]

March 3, 2026

Abstract

When neural networks (NNs) are used as a type of nonlinear parametric representation to solve partial differential equations (PDEs), they often display frequency-dependent learning dynamics that can differ from those seen in direct function approximation tasks, resulting from a balance between the frequency bias of the NN representation and that of the underlying differential operator. Although many commonly used NNs exhibit a bias towards low-frequency modes in representation, the presence of differential operators in the loss function, which amplifies high-frequency components, can lead to high frequency bias. In this work, using second order elliptic PDEs as an example, we show how these two factors compete and lead to an overall frequency bias in different situations. Once the balance is determined, it is important to design computational strategies to counter the resulting bias to improve training efficiency. We propose a simple operator-aware preconditioning strategy that rebalances the optimization landscape and the learning dynamics by applying an auxiliary integral operator to the residual. The integral kernel can be the Green's function of a reference elliptic operator or an approximation, and integrates easily with common NN solvers for PDEs. Extensive experiments, including multiscale and variable-coefficient problems, show that the approach restores more balanced learning dynamics across modes and substantially improves both convergency and accuracy.

Key words. frequency bias, preconditioner, physics-informed neural network

1 Introduction

Neural networks (NNs) provide a special form of nonlinear parametric representation for approximating functions. There are extensive results in terms of mathematical approximation theory for NNs. One of the main themes is showing universal approximation property (UAP) of NNs [Cyb89, Bar02, DHP21, KL20, LPW⁺17, ES16, SYZ22]. However, these existing mathematical results do not address the key challenges of how close and how costly one can compute the solution by solving a large-scale non-convex optimization problem using gradient-based techniques, which are sensitive to the conditioning of the parametrized representation and often become the computational bottleneck in practice.

A common feature in NN representation is the low-frequency bias. The frequency bias refers to the network's tendency to learn low-frequency components of a target function more quickly than

^{*}Department of Mathematics, City University of Hong Kong, Kowloon Tong, Hong Kong

[†]Department of Mathematics, Duke University, Durham, NC, USA

[‡]Department of Mathematics, Duke University, Durham, NC, USA

[§]Department of Mathematics and Statistics, Auburn University, Auburn, AL, USA

high-frequency ones during training, which makes it computationally more difficult and costly for networks to capture high-frequency components and fine features of target functions. This phenomenon was first systematically demonstrated by [RBA⁺19], who analyzed the Fourier spectra of neural network outputs and showed that standard architectures with ReLU or Tanh activation functions prioritize smoother, low-frequency features, even without explicit regularization. Frequency bias can be interpreted through the lens of Neural Tangent Kernel (NTK) theory, in which training dynamics are decomposed into eigenspaces of the NTK, each associated with distinct kernel eigenvalues [JGH18, CFW⁺21]. The NTK eigenvalues corresponding to high-frequency eigenfunctions decay polynomially with frequency, leading to slower learning of high-frequency components. While this implicit regularization can be beneficial for promoting smoothness, it becomes problematic when fine details or multiscale features are essential for accurate approximation. An explicit theoretical and numerical analysis [ZZZZ25c] showed ill-conditioning and frequency bias for two-layer NNs in both representation and training, due to strong correlations among parametrized global activations.

Naturally, neural networks (NNs) can be used to represent/approximate the solutions of PDEs. Numerous works have explored this approach, including Physics-Informed Neural Networks (PINNs) [RPK19, RYK20], the Deep Ritz Method (DRM) [EY18], Weak Adversarial Networks (WAN) [ZBYZ20], and among others [LJP⁺21, LKA⁺20, DRMM24]. Significant efforts have been devoted to the theoretical justification of these methods. For instance, the consistency of PINNs for linear second-order elliptic and parabolic PDEs was established in [SDK20], while the generalization error of PINNs for data assimilation was analyzed in [MM23] by examples. Analogous results for the DRM are also available [MZ19, DJL⁺22, LLW21, MZ22]. The general conclusion from these works is that, given sufficient data and appropriate handling of boundary conditions, the minimizer of the associated optimization problem converges to the solution of the PDE.

However, these theoretical guarantees often do not translate easily into practice. Although solving PDEs using NN representation can potentially offer significant advantages, such as being mesh-free, easy implementation, scalable to high dimensions, and the potential of adaptivity, the nonlinear representation has to be solved through large-scale non-convex optimization using gradient-based methods in real practice. Again, ill-conditioning and frequency bias can become problematic for numerical computations, particularly for those PDEs with solutions containing multiple frequency scales or sharp features. The presence of differential operators introduces additional factors that affect the overall ill-conditioning and frequency bias in the training process. [WWP21] recasts spectral bias in PDE solving tasks as an “NTK eigenvector bias”, and also shows that incorporating Fourier feature mappings can reshape a network’s spectral preferences, enabling better learning of the high-frequency components. In our earlier work [HLZZ25], we showed that ill-conditioning and low-frequency bias for two-layer NNs still dominate the opposite effect of a differential operator in the training dynamics. This consequence leads to numerical challenges for efficiency and accuracy compared to linear representations, such as the finite element method, with well-developed preconditioners.

In this work, we will focus on the multi-layer NNs. The story is quite different from the one for two-layer NNs. First of all, the representation capability and flexibility for multi-layer NNs are much better than two-layer NNs. In particular, its low-frequency bias can be influenced by several factors, such as network architecture, activation functions, weight initialization, and the trajectory followed by gradient descent during optimization. When trained for approximation, it is demonstrated in [BGG⁺20] and [TSM⁺20] that input encoding schemes and network depth significantly influence the frequency content learned during training. In [HSTX22], it is shown that the choice of activation function also plays a crucial role, while networks with ReLU as

activation function exhibit spectral bias connected to finite element theory, alternative activations like piecewise linear B-splines can remove this bias. Recent theoretical advances in [ZZZZ25c] demonstrate that two-layer neural networks act as ‘low-pass filters’ due to ill-conditioning of the Gram matrix, and in follow-up works [ZZZZ25b, ZZZZ25a], it is further explored that with a multi-component and multi-layer neural network (MMNN) structure, Sine activation function, and properly scaled random initialization of the first layer, NNs can be trained to approximate high-frequency modes effectively. Furthermore, properties of the optimization process, such as the evolution of sharpness [BD20] and the path traversed through the loss landscape, also modulate mode dynamics.

When using multi-layer NN representation to solve PDEs, the involvement of differential operators in the loss function, such as in PINN, which inherently introduce high frequency amplification/bias, can be a potential game changer of the overall ill-conditioning and frequency bias of the formulation and the learning dynamics. In particular, we show that, due to the flexibility, capacity, and mild frequency bias of well-designed multi-layer NNs, such as Fourier MMNNs using Sine activation function with proper initial scaling, ill-conditioning and high-frequency bias of an elliptic operator will dominate the overall formulation and the corresponding learning dynamics. As a comparison, when the finite element method is used for an elliptic PDE, since the finite element representation has no frequency bias, the ill-conditioning and high frequency bias of the resulting linear system are inherited from the differential operator. As a result, when simple iterative methods are used to solve the linear system, errors in low frequencies decay very slowly, leading to slow convergence even for smooth solutions. This is unacceptable in practice and requires the design of effective preconditioning strategies. Similarly, motivated by the observation that the underlying differential operator creates the overall frequency bias in the formulation, we propose an operator-aware preconditioning strategy that rebalances the spectral weights and training dynamics accordingly. The preconditioner is a linear operator based on a reference elliptic operator that modifies the optimization landscape, effectively reshaping the loss function to balance frequency components. This preconditioner transforms the residual before computing the loss, counteracting the frequency amplification caused by the differential operator. The preconditioner acts as a spectral filter that attenuates the differential operator-induced bias while preserving the physics constraints, accelerating the convergence to an accurate solution.

Several other approaches have been proposed to alleviate the ill-conditioning and frequency bias of PINNs. Sobolev-norm losses replace the standard squared residual with norms that include derivative information, effectively giving more weight to high-frequency components; see, for example, Sobolev-PINNs [SJHH21] and the analysis of Sobolev acceleration [LBY22]. More recently, [DRBMdB23] analyzes PINN training through an operator-conditioning lens and proposes explicit preconditioners that reduce the condition number of the composite neural tangent kernel and PDE operator. Related strategies include weighted-residual methods that use spatially-varying weight functions to balance the loss, learned preconditioners that adaptively reweight different spectral modes during training, and residual-based attention mechanisms [ATSK24] that dynamically emphasize high-residual collocation points. These strategies often require additional computational overhead, such as computing high-order derivatives, solving auxiliary eigenvalue problems, or extensive hyperparameter tuning. Different from the works above, our approach requires only the Green’s function of a simple reference operator, often available in closed form, offering a simple, effective, and interpretable mechanism to counteract the frequency bias in training process.

Our contributions include:

- Systematic study of the balance of frequency biases between a NN representation and a differential operator when solving elliptic PDEs using NNs, and show how differential operators

can dominate and result in undesirable high frequency bias and slow convergence in the training process.

- An operator-aware preconditioning strategy that reweighs frequency modes in the formulation and leads to balanced and effective learning across frequency modes.
- Comprehensive numerical experiments demonstrate that our preconditioning strategy can improve both efficiency and accuracy significantly, especially for multiscale problems.

The remainder of this paper is organized as follows. Section 2 presents the problem formulation and establishes notation for both PDE solving and function approximation tasks. Section 3 provides detailed experimental motivation, demonstrating how frequency bias manifests differently in approximation versus PDE solving, and how factors such as activation functions, network depth, and initial scaling affect spectral learning dynamics. Section 4 proposes our operator-aware preconditioner, elaborating how it modifies the gradient flow to rebalance frequency modes. Section 5 presents comprehensive numerical experiments, progressing from simple 1D cases to challenging 2D multiscale problems, demonstrating the effectiveness of our preconditioning approach. Section 6 concludes with a discussion of the implications and potential extensions of this work.

2 Problem formulation

We take second-order elliptic equations with Dirichlet boundary conditions as an example. Given a bounded domain $\Omega \subset \mathbb{R}^d$ with sufficiently smooth boundary, we consider the following partial differential equation

$$\begin{cases} Lu = f & \text{in } \Omega \\ u = g & \text{on } \partial\Omega \end{cases}. \quad (1)$$

Here, L is a second-order elliptic differential operator of the form

$$Lu = - \sum_{i,j=1}^d \frac{\partial}{\partial x_i} \left(a_{ij}(x) \frac{\partial u}{\partial x_j} \right) + c(x)u, \quad (2)$$

that is, there exists a constant $\alpha > 0$ such that

$$\sum_{i,j=1}^d a_{ij}(x) \xi_i \xi_j \geq \alpha |\xi|^2 \quad \forall x \in \Omega, \xi \in \mathbb{R}^d.$$

The function u is the unknown, and $f \in L^\infty(\Omega), g \in L^\infty(\partial\Omega)$ are given.

The main idea here is using a NN, denoted by u_θ , to represent the solution and learn the parameters θ to approximate the PDE and the boundary condition as best as possible. Although using NN representation can potentially offer a few advantages, such as being mesh-free, easy implementation, scalable to high dimensions, and the key potential of adaptivity as a nonlinear representation, the parameters have to be learned/trained through a large-scale non-convex optimization using gradient-based methods in real practice. Moreover, due to the use of nonlinear representation, an appropriate formulation of the optimization problem can be subtle, e.g., whether a strong form or weak form of the elliptic PDE problem (1) should be used and how to enforce the PDE constraint in the domain interior together with the boundary condition.

In this work, we will study the simplest and most flexible approach using the least squares formulation to enforce both the PDE and the boundary condition with a balance parameter, termed as the PINN model. The loss function $\mathcal{L}_{\text{PINN}}(\theta)$ is of the following form

$$\mathcal{L}_{\text{PINN}}(\theta) = \mathcal{L}_{\text{PINN},r}(\theta) + \lambda_b \mathcal{L}_b(\theta), \quad (3)$$

where

$$\mathcal{L}_{\text{PINN},r}(\theta) = \frac{1}{2} \int_{\Omega} |Lu_{\theta}(x) - f(x)|^2 dx = \frac{1}{2} \int_{\Omega} |L[u_{\theta}(x) - u(x)]|^2 dx, \quad (4)$$

$$\mathcal{L}_b(\theta) = \frac{1}{2} \int_{\partial\Omega} |u_{\theta}(x) - g(x)|^2 ds(x) = \frac{1}{2} \int_{\partial\Omega} |u_{\theta}(x) - u(x)|^2 ds(x). \quad (5)$$

The loss function is composed of the PDE residual term $\mathcal{L}_{\text{PINN},r}$ and the boundary fitting term \mathcal{L}_b , which is equivalent to the square of the H^2 -norm of the approximation error for L defined in (2). Here $\lambda_b > 0$ is a weighting hyperparameter balancing the two loss components.

As a comparison in our study, the most commonly used least squares formulation for direct function approximation using a NN representation is of the form

$$\mathcal{L}_{\text{approx}}(\theta) = \frac{1}{2} \int_{\Omega} |u_{\theta}(x) - u(x)|^2 dx, \quad (6)$$

which is the square of the L^2 norm of the approximation error.

In practice, these integrals are approximated by discrete sampling. For example, interior points $\{x_i^r\}_{i=1}^{N_r} \subset \Omega$ and boundary points $\{x_i^b\}_{i=1}^{N_b} \subset \partial\Omega$ are drawn randomly from uniform distributions over the domain and its boundary, respectively. The loss is then evaluated at these sampled points to approximate the continuous integral. The optimization is typically performed using gradient-based methods such as Adam [KB15] or L-BFGS, seeking

$$\theta^* = \arg \min_{\theta \in \mathbb{R}^p} \mathcal{L}_F(\theta), \quad (7)$$

for $F \in \{\text{PINN}, \text{approx}\}$.

3 Training Dynamics

Once the optimization formulation is determined, the most challenging computational task is the training process for the parameters to reach a satisfactory result. To solve this large-scale non-convex optimization problem with no clear interpretation or special structures in a very high dimensional parameter space, the training process typically relies on gradient-based optimization methods. A key issue is to understand the potential ill-conditioning in the optimization problem, which will lead to both inefficiency and bias for gradient-based methods.

We start with gradient flow using the continuous formulation. For the function approximation problem (6), the gradient flow in the parameter space is

$$\frac{d\theta}{dt} = - \int_{\Omega} \frac{\partial u_{\theta}}{\partial \theta} (u_{\theta} - u) dx, \quad (8)$$

$$\frac{d\mathcal{L}_{\text{approx}}(\theta)}{dt} = - \left\| \int_{\Omega} \frac{\partial u_{\theta}}{\partial \theta} (u_{\theta} - u) dx \right\|^2. \quad (9)$$

For function approximation using two layer NNs, it was shown in [ZZZZ25c] that strong correlations among the set of parametrized activation functions lead to ill-conditioning of the NN representation and result in low frequency bias in training and convergence. For multi-layer NNs, the situation is much more difficult to explicitly characterize and analyze since the answer depends on a more complicated composition structure as well as the choice of activation function and the initial scaling of the parameters. For example, a multi-component and multi-layer neural network structure [ZZZZ25b] using Sine activation function, called FMMNN [ZZZZ25a], with proper initial scaling was shown to have strong representation capability and flexibility through smooth composition which also leads to weak frequency bias in training.

When solving the PDE (1) using the PINN formulation (3), we have

$$\begin{aligned} \frac{d\theta}{dt} &= - \int_{\Omega} [L \frac{\partial u_{\theta}}{\partial \theta}] [L(u_{\theta} - u)] dx - \lambda_b \int_{\partial\Omega} \frac{\partial u_{\theta}}{\partial \theta} (u_{\theta} - u) ds(x), \\ \frac{d\mathcal{L}_{\text{PINN}}}{dt} &= - \left\| \int_{\Omega} [L \frac{\partial u_{\theta}}{\partial \theta}] [L(u_{\theta} - u)] dx + \lambda_b \int_{\partial\Omega} \frac{\partial u_{\theta}}{\partial \theta} (u_{\theta} - u) ds(x) \right\|^2. \end{aligned}$$

We see that the involvement of a differential operator L in the loss function (3) changes the frequency weights in the approximation error with a high frequency bias (in terms of H^2 norm). As a consequence, it changes the training dynamics as above. However, there is a subtle competition between the typical low frequency bias of a NN representation and the high frequency bias of a differential operator. The intriguing and important question is the balance between the two and the overall conditioning and frequency bias for the training dynamics when solving PDEs using a NN representation. More importantly, how to counter the frequency bias or precondition the formulation is crucial for both training efficiency and resulting accuracy.

In the recent work [HLZZ25], it was shown that, when solving elliptic PDE with a two-layer Neural network, the low-frequency bias of the NN representation still dominates. As a result, low-frequency or smooth components of the solution are captured first during the training process, while high-frequency or fine features are more costly and difficult to compute. As a conclusion, due to the low-frequency bias, using two-layer NNs is difficult to achieve the key potential of adaptivity as a nonlinear representation and is not competitive with well-developed linear method representations such as the finite element method.

In this work, we will focus on the study of using multi-layer NNs to solve elliptic PDEs of the form (1). In particular, we show that, for well-designed multi-layer NNs, which have strong representation capability and mild frequency bias, the ill-conditioning and high frequency bias of differential operators will dominate the overall formulation and lead to a nightmare for the gradient-based training process, capturing low frequency and smooth components of the solution very slowly, just as using iterative methods without preconditioning for finite element methods. To address this issue, we propose a simple and effective **operator-aware preconditioning** strategy that can improve both the efficiency and accuracy notably.

In the following, we first illustrate the behavior of frequency bias in different settings with numerical experiments. For each example, we track the evolution of the coefficients of different frequency modes in the solution error during training iterations. We then analyze the learning dynamics of these frequency modes in the neural network representation u_{θ} and examine their dependence on factors such as the activation function, network depth structure, initial scaling, and the nature of the task (e.g., function approximation or PDE solving). In the experiments presented in this section, we focus on the frequency dynamics during the early stage of training (the first 2,000 iterations). The purpose is not to analyze the plateau phase or compare architectures in terms of final accuracy, but rather to illustrate the presence of frequency bias and how frequency bias

affects the rate at which the L^2 error decreases during training. Furthermore, our experiments are conducted with over-sampled data, meaning that the sample points sufficiently resolve the target function.

3.1 Frequency bias for function approximation

In Examples 1 and 2, we examine the effects of various factors, such as activation function, initial scaling, and depth, on frequency bias in function approximation and demonstrate that reduced frequency bias generally correlates with improved convergence and accuracy.

Example 1: The goal of this example is to examine how the choice of activation functions and the initial scaling of the first layer slope parameters affect frequency bias in function approximation.

Following [ZZZZ25c], we apply an initial first-layer scaling strategy to reduce frequency bias and improve learning efficiency. After standard initialization (e.g., PyTorch’s default), the slope weights w in the activation function $\sigma(w(x - b))$ of the first layer are scaled by a factor that is proportional to $(n_1)^{\frac{1}{d}}$, where n_1 is the first layer network width and d is the input dimension. This scaling provides the largest frequency range supported by the number of neurons in the first layer, capturing diverse frequency modes in the data at the beginning of training. Subsequent layers keep standard initialization to avoid instability due to amplification across layers.

We first consider the standard fully connected neural networks (FCNN) with width 50 and depth 3, corresponding to 5,201 learnable parameters, trained for the approximation of the target function

$$u_1(x) = \sin(2\pi x) + \sin(5\pi x) + \sin(9\pi x)$$

in L^2 norm over the interval $[-1, 1]$ with 2,000 sample points. The optimization uses the Adam algorithm with a cyclic learning rate schedule, where the learning rate oscillates between a base value of $\eta_{min} = 1 \times 10^{-5}$ and a maximum value of $\eta_{max} = 2 \times 10^{-3}$. An exponential decay factor $\gamma = 0.999$ is applied to both bounds, gradually reducing the overall learning rate range throughout training.

To investigate the spectral learning behavior of the network, we study the error in different Fourier modes during training process. In this work, a frequency mode labeled by m refers to the Fourier component of the error at frequency m , measured in cycles per unit length. The analytic components of the form $\sin(k\pi x)$ correspond to frequency mode $m = k/2$. thus, the target solution components in the exact solution u_1 are associated with frequency modes 1, 2.5 and 4.5, respectively. The corresponding curve shows the evolution of the magnitude of this Fourier component over training iterations.

The results are shown in Fig. 1. We observe that, without initial scaling, the error decay is slow and Sine or Tanh as activation function does not perform as well as ReLU as activation function. This can be explained by the spectral analysis in [ZZZZ25c] for shallow NNs, i.e., the spectral decay of the Gram matrix for a family of randomly parameterized activation functions. Without scaling, the spectral decay is exponential for smooth activation functions while polynomial for ReLU. However, with a proper scaling of the slope parameters, the family of randomly parameterized activation functions provides a more diverse and less correlated basis whose Gram matrix has a slow spectral decay for a range of frequency modes that are proportional to the scaling and hence can capture more features of the underlying data as shown in [ZZZZ25c]. In particular, using properly scaled Sine in the first layer is the most efficient, like using a family of diverse random Fourier bases that are the least correlated global functions, as shown in [ZZZZ25a, TYZZ25] as well as observed in this test. Note that ReLU and its powers are invariant under scaling.

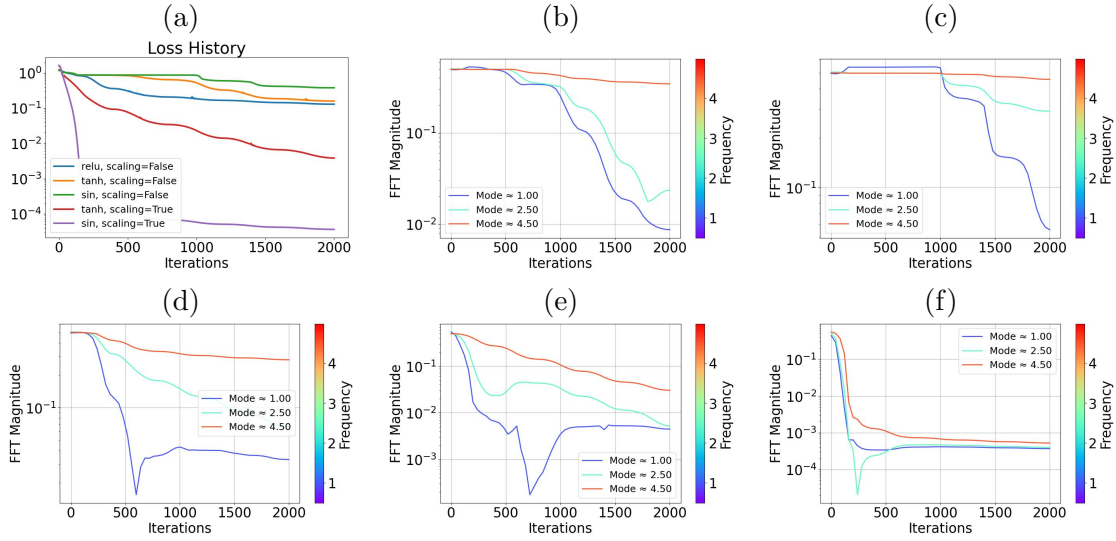


Figure 1: Example 1: Relative L^2 error and frequency bias in function approximation using different activation functions, with and without scaling. (a) Relative L^2 error during training; (b)-(f) Errors in different modes during training corresponding to activation functions Tanh, Sine, ReLU, scaled Tanh, and scaled Sine, respectively.

As for the frequency bias, we have all three NNs without scaling first layer bias towards low frequency; that is, the errors in the lower frequency modes decay faster in the training process. With scaling, NN with Sine activation function exhibits little bias towards low frequency. This also leads to a more efficient training process.

Example 2: The second test investigates how network depth influences frequency bias under otherwise similar conditions.

We use the same target function u_1 and compare three architectures: a shallow (2-layer), a 4-layer, and a 6-layer FCNN, each with a width of 100, corresponding to 301, 20,501, and 40,701 learnable parameters, respectively. For networks using Tanh or Sine activations, the same first-layer scaling is applied. The model is optimized using the Adam algorithm with a cyclic learning rate schedule, where the learning rate oscillates between a base value of $\eta_{min} = 1 \times 10^{-5}$ and a maximum value of $\eta_{max} = 1 \times 10^{-2}$, 5×10^{-3} , and 3×10^{-3} for 2-layer, 4-layer, and 6-layer NNs respectively with an exponential decay factor $\gamma = 0.999$. the total training time is approximately 16 seconds for all 2-layer networks, 20 seconds for all 4-layer networks, and 22 seconds for all 6-layer networks.

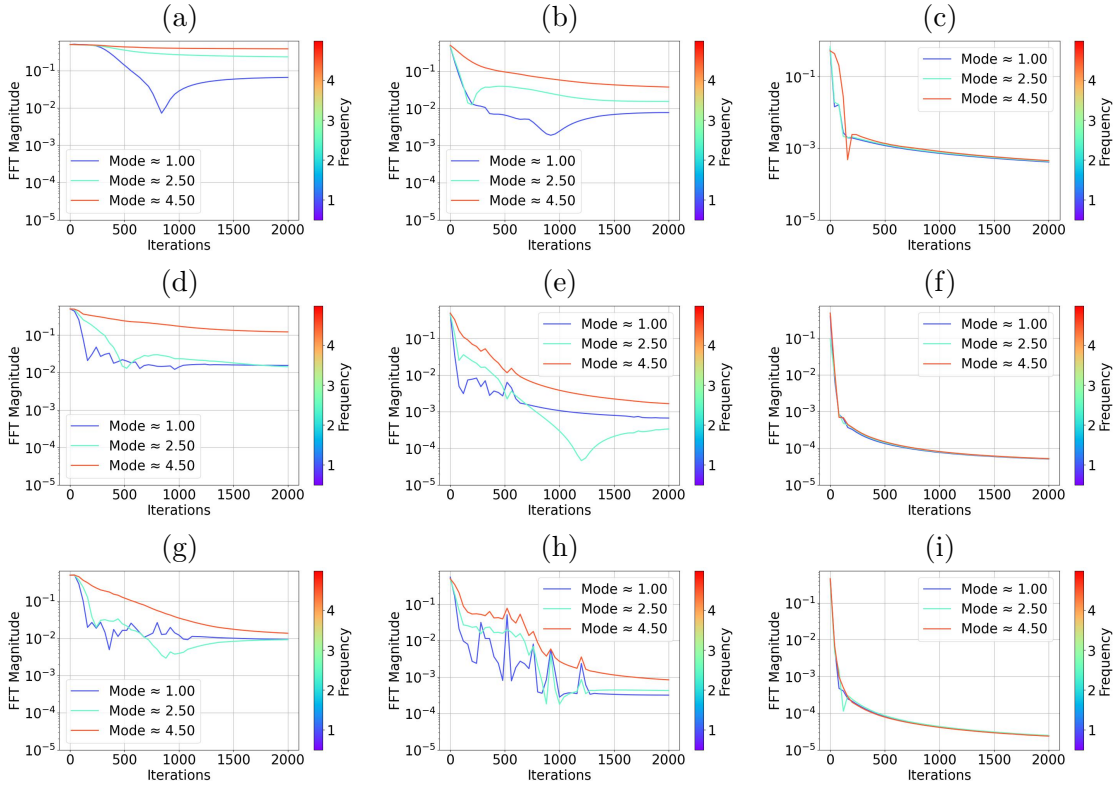


Figure 2: Example 2: Errors in different modes for a 2-layer (top row), 4-layer (middle row), and 6-layer (bottom row) neural network using ReLU (left column), Tanh (middle column), and Sine (right column) activation functions.

As the number of layers increases, the neural networks exhibit reduced frequency bias and improved overall L^2 accuracy in the early training stage. For ReLU activations (Figs. 2(a), 2(d), and 2(g)), networks with more layers show a marked reduction in frequency bias. The shallow network displays a strong bias toward low-frequency modes; that is, Mode 1 converges much faster than Mode 4.5. The 4-layer and 6-layer networks achieve more balanced learning, with all modes decaying to around 10^{-2} error within 2,000 iterations. For Tanh activations with scaling (Figs. 2(b), 2(e), and 2(h)), all models exhibit some frequency bias, but increasing the number of layers improves accuracy by roughly an order of magnitude (reaching 10^{-3} vs. 10^{-2}) and yields more uniform convergence across modes. For Sine with scaling (Figs. 2(c), 2(f), and 2(i)), the shallow network already shows good performance with minimal frequency bias, but the deep network achieves exceptional results with all modes converging to 10^{-4} error or better.

Here is the summary of a few key observations from our function approximation tests above.

- Less frequency bias leads to improved efficiency and accuracy of training process.
- The level of frequency bias depends on NN structure, activation function, and initial scaling. The increase of depth, proper initial scaling, and use of Sine activation function all lead to lesser low frequency bias and improved efficiency for function approximation.

3.2 Frequency bias in solving PDEs

We now investigate how frequency bias behaves when NNs are trained to solve PDEs, and how this behavior differs from that observed in direct function approximation. Using the Poisson equation with zero Dirichlet boundary conditions as a test case, we study the overall frequency bias for the learning dynamics in different settings.

The training dynamics in solving PDE can be significantly different from those observed in function approximation, depending on the balance between the opposite frequency biases of the differential operator and the NN representation. In other words, the presence of the differential operator alters weights for different frequency components in the error and may lead to different frequency bias during training, resulting in distinct patterns of convergence in L^2 error. When using two-layer NNs, it was shown [HLZZ25] that low frequency bias of NN representation still dominates and results in slow convergence and low accuracy of the training process when the solution contains high frequency components. However, we show below that the situation for multi-layer networks can be quite subtle and different. The more expressive a multi-layer NN is and the weaker the intrinsic frequency bias, which depends on the depth, activation function, and initial scaling as shown in the previous section, the more dominant the differential operator and its frequency bias are in the formulation and training process. Nevertheless, our tests show that, although frequency bias may vary depending on the settings, a weaker overall frequency bias still leads to improved convergence and accuracy of the training process.

In the function approximation setting, we previously examined ReLU as the activation function. For PINN, we need to use at least ReLU^3 as the activation function, which has a second derivative proportional to ReLU. Thus, we compare using ReLU^3 for both solving PDEs and function approximation.

Example 3: We employ 4-layer FCNNs with a width of 200 and 4,000 sample points for this example. The network has 81,001 learnable parameters. The exact solution u_2 to the Poisson equation is

$$u_2(x) = 1000 \chi(x) \left[\sin(60(x + 0.2)^2) e^{-80(x+0.2)^2} + 0.8 \sin(300x^2) e^{-50x^2} + 0.6 \sin(40(x - 0.2)^2) e^{-60(x-0.2)^2} \right],$$

where the smooth cutoff function $\chi(x)$ is defined as:

$$\chi(x) = \begin{cases} \exp\left(-\frac{1}{(x + 0.6)^2(0.6 - x)^2}\right), & \text{if } -0.6 < x < 0.6 \\ 0, & \text{otherwise.} \end{cases}$$

Comparing approximation using ReLU^3 (Fig. 3(b)) with PINN using ReLU^3 (Fig. 3(e)), we see that 1) the NN representation has a pretty strong low frequency bias, and 2) the frequency bias is overturned in PINN due to the overall balance between the low frequency bias of the NN representation and the prevailed high frequency bias of the differential operator. We also observe that the two opposite frequency biases almost offset each other in PINN, which leads to a better overall frequency balance in training and a faster error decay than direct function approximation in L^2 norm as shown in Fig. 3(d). Note that the relative L^2 error for PINN exhibits an oscillatory behavior because it is different from the loss function for PINN, which is equivalent to H^2 error. Actually, the overall PINN loss decreases smoothly on average, indicating that this oscillation is not caused by an excessively large learning rate.

With Sine activation function and initial scaling, the multi-layer network is much more capable in representation, which is evidenced by its minimal frequency bias as shown in Fig. 3(c) and a good

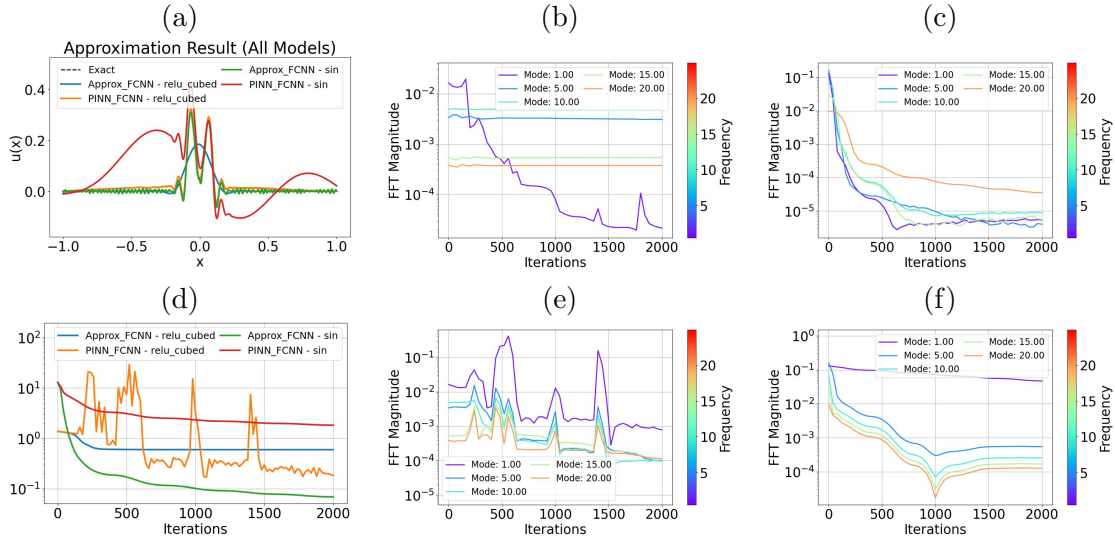


Figure 3: Example 3: Comparison of training performance and selected frequency responses. (a) Neural network outputs at 2,000 epoch for different settings; (b) Approximation using ReLU^3 activation; (c) Approximation using Sine activation; (d) Relative L^2 error history; (e) PINN with ReLU^3 activation; (f) PINN with Sine activation.

Table 1: Frequency bias in different settings (Example 3).

Task	Activation	Width/Depth	Frequency Bias	L^2 Error after 2K epochs
<i>Intrinsic Bias from Approximation</i>				
Approx	ReLU^3	200 / 4	Low freq bias	6.00E-01
Approx	Sine (scaled)	200 / 4	Minimal	6.91E-02
<i>Freq bias in PDE solving (PINN)</i>				
PINN	ReLU^3	200 / 4	Mild high freq bias	1.85E-01
PINN	Sine (scaled)	200 / 4	High freq bias	1.83E+00

approximation result as shown in Fig. 3(d). However, this means dominance from the differential operator in PINN model, which leads to a pronounced high frequency bias in the training process, as shown in Fig. 3(f) and results in a slower decay in L^2 error compared to the direct approximation as shown in Fig. 3(d).

Table 1 summarizes these observations. The numerical experiments indicate that the eventual training performance correlates with the overall frequency bias as a balance of network representation and differential operator.

Notably, we frequently observe that the PINN loss continues to decrease while the L^2 error stagnates or even grows, signaling a misalignment between the optimization objective and the target error metric. We attribute these phenomena to the frequency weighting induced by the differential operator in the PINN loss. PINNs minimize a residual norm (e.g., $\|\Delta u_\theta - f\|_{L^2(\Omega)} = \|\Delta(u_\theta - u)\|_{L^2(\Omega)} \approx \|u_\theta - u\|_{H^2(\Omega)}$), that is not directly aligned with the solution error $\|u_\theta - u\|_{L^2(\Omega)}$. In the frequency domain, a differential operator amplifies higher frequency modes, thereby emphasizing high-frequency residuals. This operator-induced bias can counteract, or even reverse the spectral tendency of the network representation, explaining the divergent behaviors noted above.

4 Operator-aware Preconditioner for PINN

Based on the insight and observation we gained in previous studies, we propose a preconditioner for PINN that would counteract the frequency bias induced by the differential operator and recover the direct function approximation metric with the help of a fixed integral kernel in the loss function.

Recall that a PINN model is trained by minimizing the loss function

$$\mathcal{L}_{\text{PINN}}(\theta) = \mathcal{L}_{\text{PINN},r}(\theta) + \lambda_b \mathcal{L}_b(\theta).$$

We propose to minimize the following loss function instead:

$$\mathcal{L}_G(\theta) = \mathcal{L}_{G,r}(\theta) + \lambda_b \mathcal{L}_b(\theta), \quad (10)$$

where

$$\begin{aligned} \mathcal{L}_{G,r}(\theta) &= \frac{1}{2} \int_{\Omega} \left| \int_{\Omega} G(x, y) [Lu_{\theta}(y) - f(y)] dy \right|^2 dx \\ &= \frac{1}{2} \int_{\Omega} \left| \int_{\Omega} G(x, y) L[u_{\theta}(y) - u(y)] dy \right|^2 dx \end{aligned} \quad (11)$$

and $G(x, y)$ denotes the Green's function for a reference elliptic operator L_0 which is spectrally equivalent to L . In practice, we choose $G(x, y)$ to be the Green's function of the Laplacian operator with either homogeneous Dirichlet boundary condition for simple domains or in free-space, for which analytical expressions are available. For the more complex operator L in equation (1), this choice still provides effective preconditioning while maintaining computational tractability, as will be demonstrated through numerical experiments.

We denote by \mathcal{G} the integral operator $\mathcal{G}f(x) := \int_{\Omega} G(x, y)f(y)dy$. The corresponding continuous gradient flow becomes

$$\begin{aligned} \frac{d\theta}{dt} &= - \int_{\Omega} [\mathcal{G}L \frac{\partial u_{\theta}}{\partial \theta}] [\mathcal{G}L(u_{\theta} - u)] dx - \lambda_b \int_{\partial\Omega} \frac{\partial u_{\theta}}{\partial \theta} (u_{\theta} - u) ds(x), \\ \frac{d\mathcal{L}_G}{dt} &= - \left\| \int_{\Omega} [\mathcal{G}L \frac{\partial u_{\theta}}{\partial \theta}] [\mathcal{G}L(u_{\theta} - u)] dx + \lambda_b \int_{\partial\Omega} \frac{\partial u_{\theta}}{\partial \theta} (u_{\theta} - u) ds(x) \right\|^2. \end{aligned}$$

We can regard $\mathcal{G}L$ as the differential operator with preconditioning. In other words, if $\mathcal{G} = L_0^{-1}$ and, L_0 and L are spectrally equivalent, $\mathcal{L}_G(\theta) \approx \|u_{\theta} - u\|_{L^2(\Omega)}$.

4.1 Implementation of the preconditioned PINN

In practical implementations, several modifications can be introduced to improve the efficiency and stability of the preconditioned PINN approach.

Truncated integral domain. Instead of performing global integration, we restrict the summation of the Green's function preconditioner to a local neighborhood around each point. Specifically, for a point $x \in \Omega$, the integration, that is, the summation in discrete form, is carried out over a ball whose radius equals the distance from x to the boundary $\partial\Omega$. The term $\mathcal{L}_{G,r}$ in the preconditioned loss function of discrete form is written as

$$\mathcal{L}_{G,r}(\theta) = \frac{1}{2N_r} \sum_{i=1}^{N_r} \left[\frac{1}{N_r} \sum_{j=1}^{M_i} G(x_i, y_{ij}) (Lu_{\theta}(y_{ij}) - f(y_{ij})) \right]^2, \quad (12)$$

where $\{x_i\}_{i=1}^{N_r}$ are the interior collocation points and $\{y_{ij}\}_{j=1}^{M_i} \subset B(x_i, r_i)$ are sample points within the ball $B(x_i, r_i)$ centered at x_i with radius $r_i = \text{dist}(x_i, \partial\Omega)$.

The reasons and benefits of the truncation are as follows. First, without truncation, allowing y_{ij} to go over the entire domain causes the integration region for points x near the boundary to be partially cut off by the domain boundary. As x approaches the boundary, this truncation becomes increasingly asymmetric, leading to growing deviation from the true Green's function and consequently to poor preconditioning. Second, this localization reduces computational cost and, most importantly, can still capture the singularity of the Green's function, which determines high-frequency asymptotics of the differential operator and hence maintains a good preconditioning effect. Moreover, the localization is adaptive to the distance to the boundary, which can capture the most influential boundary condition. The effect of this truncation is analyzed in detail in Subsection 4.2.

The formulation (12) is a discrete approximation of the continuous integral operator. In particular, the distribution of x_i and y_{ij} determines the discretization error. In our tests, we choose our collocation points on a grid for both x_i and y_{ij} . So, the spectral property of the kernel can be maintained accurately for frequency modes that can be resolved well by the underlying grid. We remark that, since a NN representation allows evaluation and differentiation at any point, x_i and y_{ij} can be sampled freely. One can potentially design more efficient and accurate adaptive sampling around each x_i accordingly. This meshless representation is more helpful for complicated geometry and in high dimensions.

Boundary condition. It is well-known that one challenge in designing the loss function for the standard PINN model (3) is the proper balance between the PDE residue term \mathcal{L}_r in the domain interior and the boundary error term \mathcal{L}_b . Actually, this balance is solution-dependent. Take the Dirichlet boundary condition as an example, \mathcal{L}_r is the approximation error involving the second derivatives of the solution, while \mathcal{L}_b is the approximation error of the solution on the boundary. In particular, if the solution has multiple scales, it is difficult to choose a constant λ_b to achieve a proper balance. For Dirichlet boundary condition, this is straightforward for the preconditioned PINN model (10), since $\mathcal{L}_{G,r}(\theta) \approx \|u_\theta - u\|_{L^2(\Omega)}$, if $G = L_0^{-1}$ and L_0 is spectrally equivalent to L . So as long as λ_b balances the sampling density at the boundary and in the interior properly, the two terms are well-matched and $\mathcal{L}_G(\theta) \approx \|u_\theta - u\|_{L^2(\bar{\Omega})}$, where $\bar{\Omega} = \Omega \cup \partial\Omega$. In this work, we set the regularization parameter in the preconditioned loss function to 1 in all numerical experiments. We also observe that the performance is not sensitive to the choice of this parameter when preconditioning is applied.

Computation Cost. Using an integral operator introduces an extra summation operation. This summation can be accelerated using the fast multi-pole method (FMM) [GR87, YBZ04] or a hierarchical hemi-separable (HHS) [CGP06, CGP06] sparsification of the kernel in general. However, in practice, this added summation cost is insignificant compared to the computation cost of taking derivatives of a NN representation and the backpropagation operation in each training step. Hence, the computation cost for the preconditioned PINN and the standard PINN is comparable as shown in our numerical tests.

We present extensive numerical experiments, from 1D examples to 2D multi-scale problems, to demonstrate significant acceleration of convergence and improvement of accuracy when preconditioning is applied. Moreover, the preconditioning framework works on top of any network structure and improves their performance. For 1D problems, we use FCNNs as the network representation. For more challenging 2D problems, we employ a multi-component and multi-layer neural network (MMNN) architecture introduced in [ZZZZ25a, ZZZZ25b] to represent the solution u_θ . While an easy modification to FCNNs through the introduction of balanced multi-component structures in

the network - the number of components in each layer, called the rank, is much smaller than the network width, MMNNs achieve a significant reduction of training parameters, a much more efficient training process, and a much improved accuracy compared to FCNNs, especially for functions with complex features. Such architectures improve scalability in terms of network width and depth for high-dimensional problems, making the preconditioned PINN more practical for large-scale applications. We will showcase in Example 6(a) and 6(b) that for the same PDE, using the MMNN architecture can reach the same level of accuracy with one order of magnitude fewer learnable parameters than FCNN. For all network structures, we use Sine activation function and initial scaling to improve the representation capability and reduce the frequency bias of NN representations. Moreover, a network using Sine as the activation function can be differentiated as many times as needed. The combination of these NN setups and the preconditioning strategy allows us to solve PDEs almost as direct function approximation in terms of efficiency and accuracy.

4.2 Effective norm of the preconditioned loss term

In this subsection, we analyze the continuous form of the preconditioned loss $\mathcal{L}_{G,r}$ in (12), and show that with the truncated integral domain, this term is weaker than $\|L(u_\theta - u)\|_{H^{-1+\varepsilon}(\Omega)}^2$ for any sufficiently small $\varepsilon > 0$. It essentially means the loss function retrieves at least $(1 - \varepsilon)$ derivative back from $L(u_\theta - u)$. Moreover, if we can have a uniform estimate of the decay of the Fourier transform of $L(u_\theta - u)$, it is possible to retrieve $3/2$ derivatives for the loss function.

Lemma 4.1. *Let $\Phi_d(r) = \log(r)$ for $d = 2$ and $\Phi_d(r) = \sqrt{\frac{2}{\pi}} \frac{1}{r}$ for $d = 3$. Define $\mathcal{A}_d(\rho, \ell)$, $\ell \in [0, 1]$, as follows:*

$$\begin{aligned} \mathcal{A}_d(\rho, \ell) &:= \rho^{-\frac{d-2}{2}} \int_0^\ell \Phi_d(r) J_{\frac{d-2}{2}}(\rho r) r^{\frac{d-2}{2}} r dr \\ &= \begin{cases} \frac{1}{\rho^2} (1 - J_0(\rho\ell) - \log(\ell)\rho\ell J_1(\rho\ell)), & d = 2, \\ \frac{1}{\rho^2} (1 - \cos(\rho\ell)), & d = 3, \end{cases} \end{aligned}$$

where J_ν is the Bessel function of the first kind of order ν . Then there is an absolute constant $C_{\mathcal{A}} > 0$ that

$$|\mathcal{A}_d(\rho, \ell)| \leq \begin{cases} C_{\mathcal{A}} \min(1, \rho^{-3/2}), & d = 2 \\ C_{\mathcal{A}} \min(1, \rho^{-2}), & d = 3. \end{cases}$$

for all $\rho \geq 0$.

Proof. When $d = 2$, for $x \in [0, 1]$, $J_0(x) = 1 + \mathcal{O}(x^2)$ and $J_1(x) = \mathcal{O}(x)$. For $x > 1$, we use the asymptotic approximation for $k = 0, 1$ in [Kra14] that

$$J_k(x) = \sqrt{\frac{2}{\pi x}} \cos\left(x - \frac{k\pi}{2} - \frac{\pi}{4}\right) + \mathcal{O}\left(\frac{|k^2 - \frac{1}{4}|}{x^{3/2}}\right),$$

which concludes the desired estimate by letting $x = \rho\ell$. Notice that $\ell^2 |\log \ell| \leq \ell |\log \ell|$ is uniformly bounded on $\ell \in [0, 1]$.

When $d = 3$, we have $1 - \cos(\rho\ell) = \mathcal{O}((\rho\ell)^2)$ when $\rho\ell \in [0, 1]$ and if $\rho\ell > 1$, we use $|1 - \cos(\rho\ell)| = \mathcal{O}(1)$. \square

Theorem 4.2. *Let $\Omega = B(0, 1)$ be the unit disc in \mathbb{R}^d , $d = 2, 3$, and $\ell(x) = \text{dist}(x, \partial\Omega) = 1 - |x|$. Denote χ be the characteristic function in the unit disc and*

$$G_d(x) = \begin{cases} -\frac{\log|x|}{2\pi}, & d = 2, \\ -\frac{1}{4\pi|x|}, & d = 3, \end{cases}$$

be the Green's function of the Laplacian in free space. Define

$$\mathcal{T}f(x) := \int_{\mathbb{R}^2} \chi\left(\frac{x-y}{\ell(x)}\right) G(x-y)f(y)dy.$$

1. Let $f \in H^s(\Omega)$, then for any $\varepsilon > 0$, there exists a constant C_ε that

$$\|\mathcal{T}(I - \Delta)^s f\|_{L^2(\Omega)} \leq C_\varepsilon \|f\|_{H^{s-(1-\varepsilon)}(\Omega)},$$

2. Let $\widehat{f}(\xi)$ be the Fourier transform of f . Suppose

$$\widehat{f}(\xi) = \begin{cases} \sum_{k=-\infty}^{\infty} c_k(|\xi|)e^{ik \arg(\xi)}, & d = 2, \\ \sum_{k=0}^{\infty} \sum_{l=-k}^k c_{k,l}(|\xi|)Y_{kl}\left(\frac{\xi}{|\xi|}\right), & d = 3, \end{cases}$$

satisfies that

$$\begin{aligned} |c_\alpha(|\xi|)| &\leq D\gamma(\alpha)(1 + |\xi|^2)^{-\frac{s}{2}-\delta-\frac{d-2}{2}}, \\ |c_\alpha(|\xi|)| &\leq \gamma(\alpha) \left(\sum_{\beta} |c_\beta(|\xi|)|^2 \right)^{1/2}, \end{aligned}$$

where α, β represent the multi-subscripts in $d = 2$ or $d = 3$, Y_{kl} is the spherical harmonics, D is a constant, $\delta > 0$, and $\sum_{\beta} |\gamma(\beta)|^2 < \infty$. Then there exists $p \in (2, \infty)$ and a constant $C' > 0$ that

$$\|\mathcal{T}(I - \Delta)^s f\|_{L^2(\Omega)} \leq C' \|f\|_{B,s,p}^{(p-2)/p} \|f\|_{H^{s-3/2}(\Omega)}^{2/p},$$

where the norm

$$\|f\|_{B,s,p} := \left(\int_0^\infty \left| (1 + |\xi|^2)^{s-(2-\frac{d}{2})} \sum_{\alpha} |c_\alpha(\xi)|^2 \right|^{\frac{p-2}{2(p-1)}} d|\xi| \right)^{\frac{p-1}{p-2}}.$$

Proof. Let $\phi \in L^2(\Omega)$, then

$$\begin{aligned} &\int_{\Omega} \left| \int_{\mathbb{R}^2} \chi\left(\frac{x-y}{\ell(x)}\right) G_d(x-y)\phi(y)dy \right|^2 dx \\ &= \int_{\Omega} \left| \int_{\mathbb{R}^2} \chi\left(\frac{x-y}{\ell(x)}\right) G_d(x-y) \int_{\mathbb{R}^2} \widehat{\phi}(\xi)e^{i\pi\xi \cdot y} dy \right|^2 dx \\ &= \int_{\Omega} \left| \int_{\mathbb{R}^2} \widehat{\phi}(\xi) \left(\int_{\mathbb{R}^2} \chi\left(\frac{x-y}{\ell(x)}\right) G_d(x-y)e^{i\xi \cdot y} dy \right) d\xi \right|^2 dx \\ &= \int_{\Omega} \left| \int_{\mathbb{R}^2} \widehat{\phi}(\xi)e^{i\xi \cdot x} \mathcal{A}_d(|\xi|, \ell(x)) d\xi \right|^2 dx \\ &= \int_{\mathbb{R}^2} \int_{\mathbb{R}^2} \mathcal{H}_d(\xi, \zeta) \widehat{\phi}(\xi) \overline{\widehat{\phi}(\zeta)} d\xi d\zeta. \end{aligned}$$

The kernel function

$$\begin{aligned}\mathcal{H}_d(\xi, \zeta) &= \int_{\Omega} \mathcal{A}_d(|\xi|, \ell(x)) \mathcal{A}_d(|\zeta|, \ell(x)) e^{i(\xi - \zeta) \cdot x} dx \\ &= \begin{cases} 2\pi \int_0^1 \mathcal{A}_d(|\xi|, 1-r) \mathcal{A}_d(|\zeta|, 1-r) J_0(|\xi - \zeta|r) r dr, & d = 2, \\ (2\pi)^{3/2} \int_0^1 \mathcal{A}_d(|\xi|, 1-r) \mathcal{A}_d(|\zeta|, 1-r) \frac{J_{1/2}(|\zeta - \xi|r)}{\sqrt{|\zeta - \xi|r}} r^2 dr, & d = 3, \end{cases} \quad (13)\end{aligned}$$

where J_ν denotes the Bessel function of the first kind at order ν . Next, we reformulate (13) by Graf's and Gegenbauer's addition formula

$$\begin{aligned}J_0(|\zeta - \xi|r) &= \sum_{k=-\infty}^{\infty} J_k(|\xi|r) J_k(|\zeta|r) C_k^{(0)}(\cos \theta), \\ \frac{J_{1/2}(|\zeta - \xi|r)}{\sqrt{|\zeta - \xi|r}} &= \sqrt{\frac{\pi}{2}} \sum_{k=0}^{\infty} (2k+1) J_{k+1/2}(|\xi|r) J_{k+1/2}(|\zeta|r) C_k^{(1/2)}(\cos \theta),\end{aligned}$$

where θ is the angle between ξ and ζ , $C_k^{(0)}$ and $C_k^{(1/2)}$ are Gegenbauer polynomials. Then we obtain a decomposition for $d = 2, 3$:

$$\begin{aligned}\mathcal{H}_d(\xi, \zeta) &= \begin{cases} 2\pi \sum_{k=-\infty}^{\infty} \mathcal{H}_{d,k}(|\xi|, |\zeta|) C_k^{(0)}(\cos \theta), & d = 2, \\ 2\pi^2 \sum_{k=0}^{\infty} (2k+1) \mathcal{H}_{d,k}(|\xi|, |\zeta|) C_k^{(1/2)}(\cos \theta), & d = 3, \end{cases} \\ \mathcal{H}_{d,k}(|\xi|, |\zeta|) &= \begin{cases} \int_0^1 \mathcal{A}_d(|\xi|, 1-r) \mathcal{A}_d(|\zeta|, 1-r) J_k(|\xi|r) J_k(|\zeta|r) r dr, & d = 2, \\ \int_0^1 \mathcal{A}_d(|\xi|, 1-r) \mathcal{A}_d(|\zeta|, 1-r) J_{k+1/2}(|\xi|r) J_{k+1/2}(|\zeta|r) r^2 dr, & d = 3. \end{cases}\end{aligned}$$

By Lemma 4.1, $\mathcal{H}_{d,k}(|\xi|, |\zeta|)$ is uniformly bounded for all ξ, ζ and k . For $|\nu| \leq \frac{1}{2}$, it is known that $|J_\nu(\rho r)| \leq \sqrt{\frac{2}{\pi \rho r}}$ [Sze39, Theorem 7.31.2]. Hence, there exists an absolute constant C that $|\mathcal{H}_{d,0}(|\xi|, |\zeta|)| \leq \frac{C}{|\xi|^{(d+2)/2} |\zeta|^{(d+2)/2}}$ for $d = 2, 3$. For $|\nu| \geq 1$, we use the estimate from [Kra14], $|J_\nu(\rho r)| \leq \sqrt{\frac{2}{\pi}} |\rho^2 r^2 - \omega_\nu^2|^{-1/4}$, $\omega_\nu^2 = \nu^2 - \frac{1}{4}$. Then, take $\omega = \omega_k$ or $\omega = \omega_{k+1/2}$, we have the estimate

$$\begin{aligned}|\mathcal{H}_{d,k}(|\xi|, |\zeta|)| &\leq \frac{C_{\mathcal{A}}^2}{|\xi|^{(d+2)/2} |\zeta|^{(d+2)/2}} \int_0^1 \frac{r}{|r^2 - (\frac{\omega}{|\xi|})^2|^{1/4} |r^2 - (\frac{\omega}{|\zeta|})^2|^{1/4}} dr \\ &\leq \frac{C_{\mathcal{A}}^2}{|\xi|^{(d+2)/2} |\zeta|^{(d+2)/2}} \int_0^1 \frac{\sqrt{r}}{|r - \frac{\omega}{|\xi|}|^{1/4} |r - \frac{\omega}{|\zeta|}|^{1/4}} \frac{\sqrt{r}}{|r + \frac{\omega}{|\xi|}|^{1/4} |r + \frac{\omega}{|\zeta|}|^{1/4}} dr \\ &\leq \frac{C_{\mathcal{A}}^2}{|\xi|^{(d+2)/2} |\zeta|^{(d+2)/2}} \int_0^1 \frac{\sqrt{r}}{|r - \frac{\omega}{|\xi|}|^{1/4} |r - \frac{\omega}{|\zeta|}|^{1/4}} dr \\ &\leq \frac{C}{|\xi|^{(d+2)/2} |\zeta|^{(d+2)/2}}.\end{aligned}$$

Therefore, combined with the uniform boundedness of $\mathcal{H}_{d,k}$, we have the bound

$$|\mathcal{H}_{d,k}(|\xi|, |\zeta|)| \leq \frac{C'}{(1 + |\xi|^2)^{(d+2)/4}(1 + |\zeta|^2)^{(d+2)/4}}$$

for some absolute constant $C' > 0$. For any $f \in H^s(\Omega)$, we take $\phi = (I - \Delta)^{s/2} f \in L^2(\Omega)$, then

$$\widehat{\phi}(\xi) = \begin{cases} \sum_{k=-\infty}^{\infty} (1 + |\xi|^2)^{s/2} c_k(|\xi|) e^{ik \arg(\xi)}, & d = 2, \\ \sum_{k=0}^{\infty} \sum_{l=-k}^k (1 + |\xi|^2)^{s/2} c_{k,l}(|\xi|) Y_{kl} \left(\frac{\xi}{|\xi|} \right), & d = 3, \end{cases}$$

where Y_{kl} denotes the spherical harmonics on \mathbb{S}^{d-1} . Then, denote $\Theta(|\xi|, |\zeta|) = (1 + |\xi|^2)(1 + |\zeta|^2)$, use Cauchy-Schwartz inequality,

$$\begin{aligned} & \int_{\mathbb{R}^d} \int_{\mathbb{R}^d} \mathcal{H}_d(\xi, \zeta) \widehat{\phi}(\xi) \overline{\widehat{\phi}(\zeta)} d\xi d\zeta \\ & \asymp \begin{cases} \sum_{k=-\infty}^{\infty} \iint_{\mathbb{R}_+^2} \mathcal{H}_{d,k}(|\xi|, |\zeta|) \Theta(|\xi|, |\zeta|)^{s/2} c_k(|\xi|) \overline{c_k(|\zeta|)} |\zeta|^{d-1} |\xi|^{d-1} d|\zeta| d|\xi|, & d = 2 \\ \sum_{k=0}^{\infty} \sum_{l=-k}^k \iint_{\mathbb{R}_+^2} \mathcal{H}_{d,k}(|\xi|, |\zeta|) \Theta(|\xi|, |\zeta|)^{s/2} c_{k,l}(|\xi|) \overline{c_{k,l}(|\zeta|)} |\zeta|^{d-1} |\xi|^{d-1} d|\zeta| d|\xi|, & d = 3 \end{cases} \\ & \leq C' \sum_{\alpha} \left(\int_0^{\infty} (1 + |\xi|^2)^{\frac{s}{2} - \frac{d+2}{4}} |c_{\alpha}(|\xi|)| |\xi|^{d-1} d|\xi| \right)^2 \\ & \leq C' \sum_{\alpha} \left(\int_0^{\infty} \frac{1}{(1 + |\xi|^2)^{\frac{d}{2} + \varepsilon}} |\xi|^{d-1} d|\xi| \right) \left(\int_0^{\infty} (1 + |\xi|^2)^{s-1+\varepsilon} |c_{\alpha}(|\xi|)|^2 |\xi|^{d-1} d|\xi| \right) \\ & \asymp \|f\|_{H^{s-(1-\varepsilon)}}^2, \end{aligned}$$

where we use α to represent all possible subscripts in the summation for both $d = 2$ and $d = 3$. For the second part, we adopt the Hölder inequality instead of the Cauchy-Schwartz inequality in the last step. Using the controlled decay rates of $|c_k(|\xi|)|$ in the theorem, we obtain

$$\begin{aligned} & \sum_{\alpha} \left(\int_0^{\infty} (1 + |\xi|^2)^{\frac{s}{2} - \frac{d+2}{4}} |c_{\alpha}(|\xi|)| |\xi|^{d-1} d|\xi| \right)^2 \\ & \leq \sum_{\alpha} \left(\int_0^{\infty} \left| (1 + |\xi|^2)^{\frac{s-1}{2}} |c_{\alpha}(\xi)| \right|^{\frac{p-2}{p-1}} d|\xi| \right)^{2(p-1)/p} \left(\int_0^{\infty} (1 + |\xi|^2)^{s-3/2} |c_{\alpha}(\xi)|^2 |\xi|^{d-1} d|\xi| \right)^{2/p} \\ & \leq C'' \left(\int_0^{\infty} \left| (1 + |\xi|^2)^{s-(2-\frac{d}{2})} \sum_{\alpha} |c_{\alpha}(|\xi|)|^2 \right|^{\frac{p-2}{2(p-1)}} d|\xi| \right)^{2(p-1)/p} \|f\|_{H^{s-3/2}(\Omega)}^{4/p} \\ & = C'' \|f\|_{B,s,p}^{2(p-2)/p} \|f\|_{H^{s-3/2}(\Omega)}^{4/p}, \end{aligned}$$

where $C'' = \sum_{k=-\infty}^{\infty} \gamma_k^2 < \infty$, and when p is sufficiently large, $\|f\|_{B,s,p}$ is finite. \square

5 Numerical Experiments

In this section, we investigate the performance of the preconditioned PINN under a range of problem settings to assess the effectiveness of the proposed preconditioning strategy. Examples 4–5 consider one-dimensional Poisson equations. Examples 6(a)–(b) examine a one-dimensional elliptic equation with variable coefficients. Examples 7 and 8 study two-dimensional Poisson equations with homogeneous and nonhomogeneous Dirichlet boundary conditions, respectively, while Example 9 addresses a two-dimensional elliptic equation with variable coefficients. Example 10 examines the three-dimensional Poisson equations. For all examples, we use full batch training and the activation function is chosen to be Sine, with the weights of the first layer scaled proportional to $(n_1)^{\frac{1}{d}}$, where n_1 is the first layer network width and d is the input dimension.

When implementing the preconditioned loss formulation (10), for all one-dimensional examples in the domain $\Omega = (-1, 1)$, we compute $\mathcal{L}_{G,r}$ of the form (11) by choosing G as the Green’s function for the Laplacian with homogeneous Dirichlet boundary conditions, which has the analytical expression:

$$G(x, y) = \begin{cases} \frac{1}{2}(1-y)(1+x), & \text{if } x \leq y \\ \frac{1}{2}(1-x)(1+y), & \text{if } x > y. \end{cases}$$

For the two-dimensional ($d = 2$) and three-dimensional ($d = 3$) problems in domains of different shapes, we implement the truncated integral form in (12) and select the function G in the preconditioned formulation to be the Green’s function of the Poisson equation in free space, given by

$$G(x, y) = \begin{cases} -\frac{1}{2\pi} \log(|x - y|), & d = 2, \\ -\frac{1}{4\pi|x-y|}, & d = 3. \end{cases}$$

In examples below, we implement the preconditioned PINN to solve PDEs, compare with PINN without preconditioning and function approximation, plot the L^2 errors, and present the dynamics of selected frequency modes in errors.

Example 4: We solve the Poisson equation with homogeneous Dirichlet boundary conditions, where the force term f is chosen such that $u_1(x) = \sin(2\pi x) + \sin(5\pi x) + \sin(9\pi x)$ is the exact solution. An FCNN with width 50 and depth 3, corresponding to 5,251 learnable parameters, is used to represent the solution. The model is trained using 2,000 collocation points.

Fig. 4 presents the comparison between standard PINN, preconditioned PINN (labeled as *kernelG_PINN_FCNN* in the legend), and direct function approximation. Indeed, we observe that the frequency modes dynamic for the preconditioned PINN is very similar to that for function approximation. The decaying rate of the L^2 error is also much better than the PINN formulation without preconditioning and comparable to the direct approximation. The training times are 16 seconds for direct function approximation, and 24 and 26 seconds for the standard PINN and the preconditioned PINN, respectively. Despite the slight additional cost, the preconditioning strategy effectively mitigates the high-frequency bias induced by the differential operator in the standard PINN formulation, restoring balance across frequency modes and improving both convergence and training accuracy.

Example 5: We solve the Poisson equation with homogeneous Dirichlet boundary conditions, and the exact solution is the localized function u_2 in Example 3, which contains fine features and high frequency modes. We use an FCNN with width 200 and depth 3, maintaining the same training configuration as Example 4.

In this example, the errors in selected frequency modes 1.0, 5.0, 10.0, 15.0, and 20.0, are shown in Fig. 5, representing a broader range than in Example 4. Since the localized function u_2

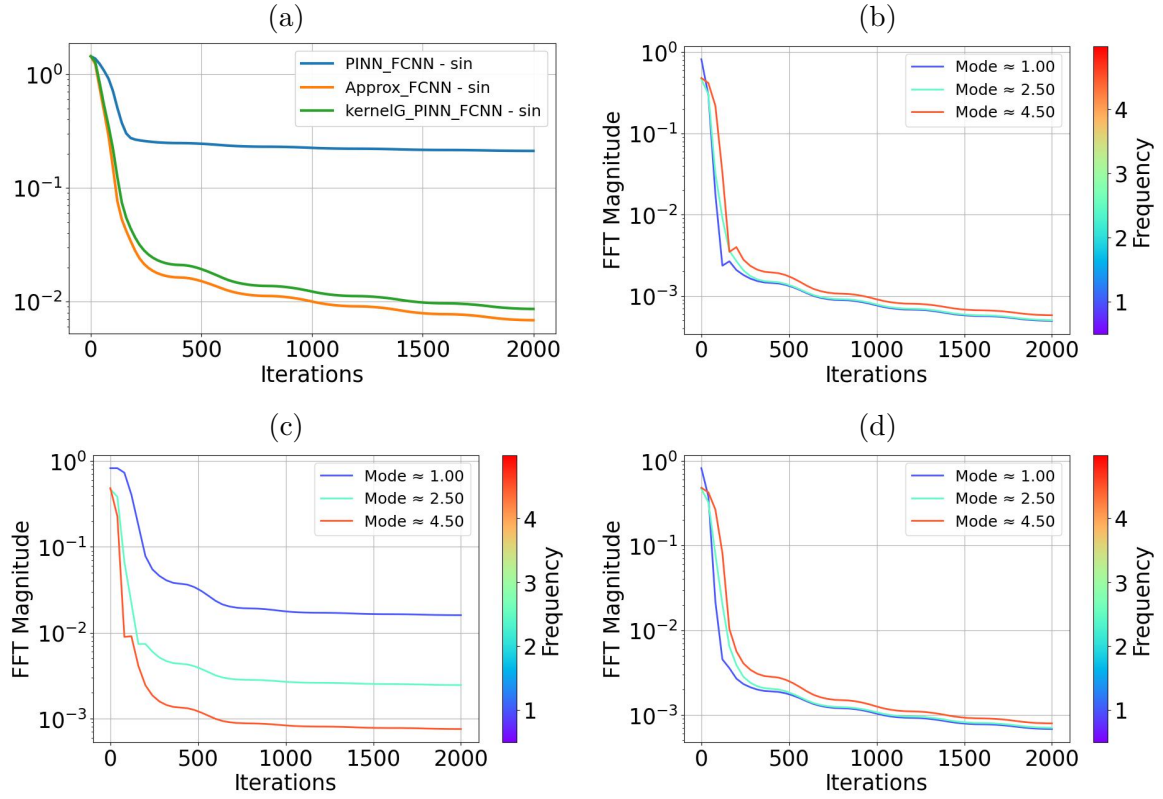


Figure 4: Example 4: Comparison of L^2 error and errors in selected frequency modes in training for different models. (a) Training loss for all models; (b) Function Approximation; (c) PINN; (d) Preconditioned PINN.

contains quite high-frequency components, using a relatively shallow neural network for function approximation still shows mild low frequency bias and requires more iterations to capture the frequency mode 20, as shown in Fig. 5(b). However, Fig. 5(c) shows that, for the standard PINN, the presence of the differential operator changes the picture completely due to reweighting the frequency modes in the loss function and placing more emphasis on high-frequency components. As a result, it leads to strong high frequency bias and slow convergence of smooth components in training, which is unacceptable in real practice (similar to using finite element methods for elliptic PDEs without a preconditioner). In contrast, the preconditioned PINN exhibits frequency mode dynamics that are nearly identical to those of the direct function approximation and consequently achieves much improved efficiency and accuracy in training. The training times are 32 seconds for direct function approximation and are comparable for the standard PINN and the preconditioned PINN (38 and 41 seconds, respectively). The tests again demonstrate the effectiveness of our proposed preconditioning strategy.

Example 6(a): We consider an elliptic PDE with a rapidly oscillating variable coefficient:

$$\begin{cases} \nabla \cdot (k(x)\nabla u) = -1 & \text{in } \Omega \\ u = 0 & \text{on } \partial\Omega \end{cases}, \quad (14)$$

where

$$k(x) = \frac{2}{2 + A \sin\left(\frac{2\pi x}{\varepsilon}\right)} + 2 + A \cos\left(\frac{2\pi x}{\varepsilon}\right). \quad (15)$$

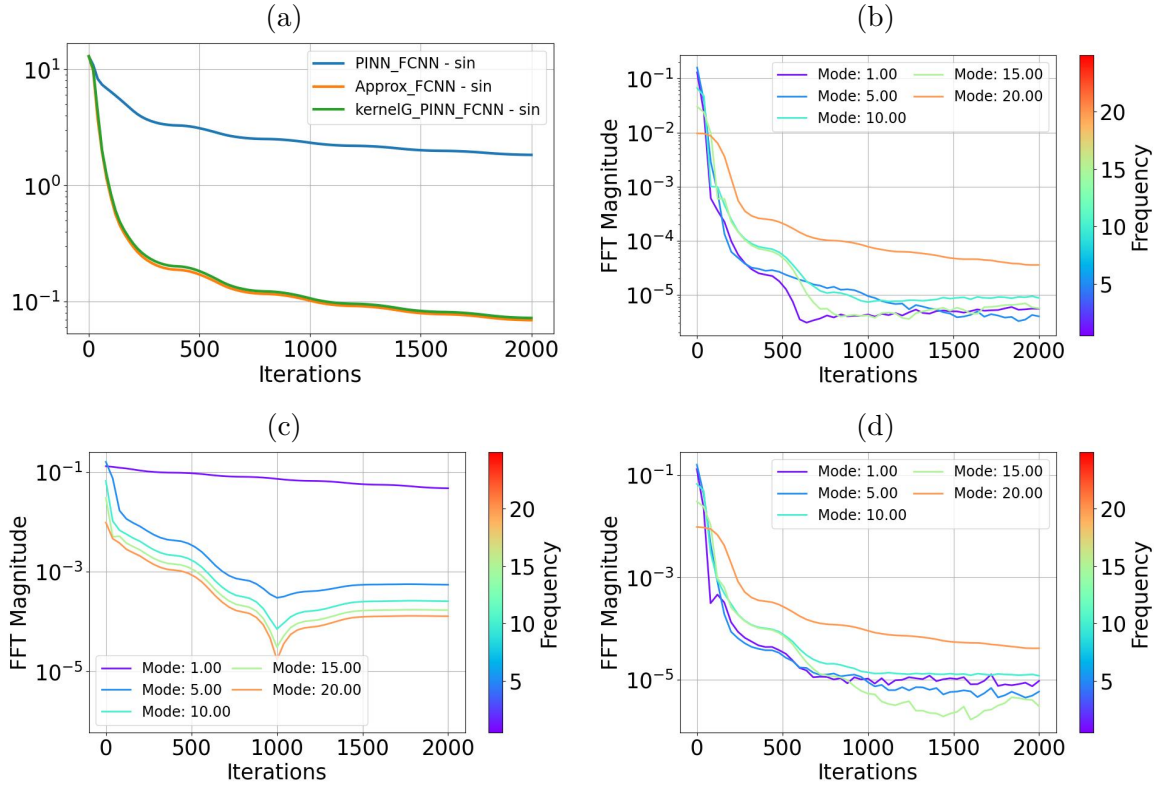


Figure 5: Example 5: Comparison of L^2 error and errors in selected frequency modes in training for different models. (a) Training loss for all models; (b) Function approximation; (c) PINN; (d) Preconditioned PINN.

In this test, we take $A = 1.8$ and $\varepsilon = 0.1$ which creates a rapidly oscillating diffusion coefficient with period ε , leading to a solution with both slow global variations and fast local oscillations, which is a classical homogenization problem. We use a FCNN of width 100 and depth 3, corresponding to 20,501 learnable parameters, to represent the solution.

This example is particularly challenging for PINNs due to the multiscale nature of the solution. We observe that the standard PINN suffers from strong high frequency bias and struggles to capture the low-frequency modes, resulting in a large relative L^2 error even after 20,000 epochs, with the error decaying very slowly. Despite the fact that the reference differential operator Δ differs from the exact differential operator in the equation, the frequency bias is well alleviated by the preconditioner, showing much less high frequency bias as reflected in the mode dynamics 6(d). This reduction in frequency bias is accompanied by a notable improvement in overall accuracy. Specifically, the relative L^2 error for the standard PINN with an FCNN is 9.61×10^{-1} , while the preconditioned PINN reduces the error to 1.80×10^{-2} . For comparison, the direct function approximation model using an FCNN achieves a relative L^2 error of 1.88×10^{-3} .

Example 6(b): In this example, we evaluate the use of a Fourier MMNN [ZZZZ25a] (FMMNN) with width 50, rank 20, and depth 3 for function approximation or to solve the same variable coefficient equation from Example 6(a).

Similar phenomena as in Example 6(a) are observed. The MMNN architecture achieves the same level of accuracy with significantly fewer learnable parameters, with 2,091 parameters compared to 20,501 parameters for the FCNN, which is approximately a tenfold reduction. Despite

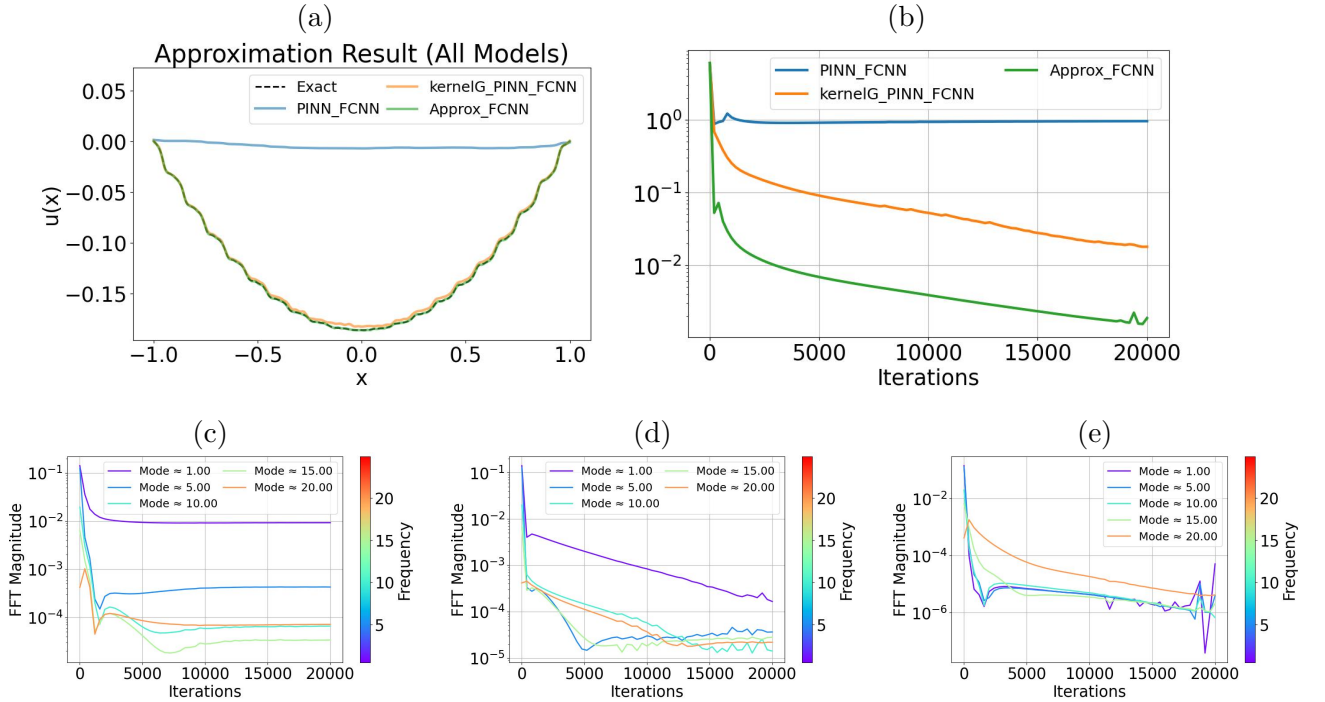


Figure 6: Example 6(a): (a) Exact solution and numerical results using FCNN; (b) L^2 relative error history; Errors in selected modes for PINN (c), preconditioned PINN (d), and approximation (e).

this substantial decrease in model size, the same qualitative trends persist. In particular, the standard PINN with an MMNN exhibits a large relative L^2 error of 9.78×10^{-1} , while the preconditioned PINN reduces the error to 3.07×10^{-2} . For comparison, the MMNN-based approximation model achieves a relative L^2 error of 4.16×10^{-3} . This demonstrates that architectural innovations and preconditioning are complementary strategies for improving PINN performance, regardless of whether an FCNN or MMNN is employed.

As demonstrated in Example 6, the MMNN architecture is able to achieve comparable accuracy with significantly fewer learnable parameters. We adopt the MMNN architecture for all subsequent two-dimensional numerical experiments.

In the two-dimensional setting, the frequency bias is analyzed using a two-dimensional discrete Fourier transform of the error. Each Fourier coefficient corresponds to a pair of frequency modes (k_x, k_y) in the x - and y -directions respectively. To visualize the frequency-dependent learning dynamics, we track a selected set of Fourier modes $(k_x, k_y) = (1, 0), (2, 0), (3, 0), (4, 0)$, which correspond to oscillations along the x -direction. Monitoring the errors in these modes over training iterations enables direct comparison with the one-dimensional frequency analysis. At the same time, the spatial error will also be plotted to offer a global view of the approximation quality and reveal error patterns in the learned solution. Together, the selected mode dynamics and spatial error visualization provide complementary insight into frequency bias in the two-dimensional setting.

Example 7: We solve the Poisson equation $\Delta u = -f$ in $\Omega = [-1, 1] \times [-1, 1]$ with homogeneous

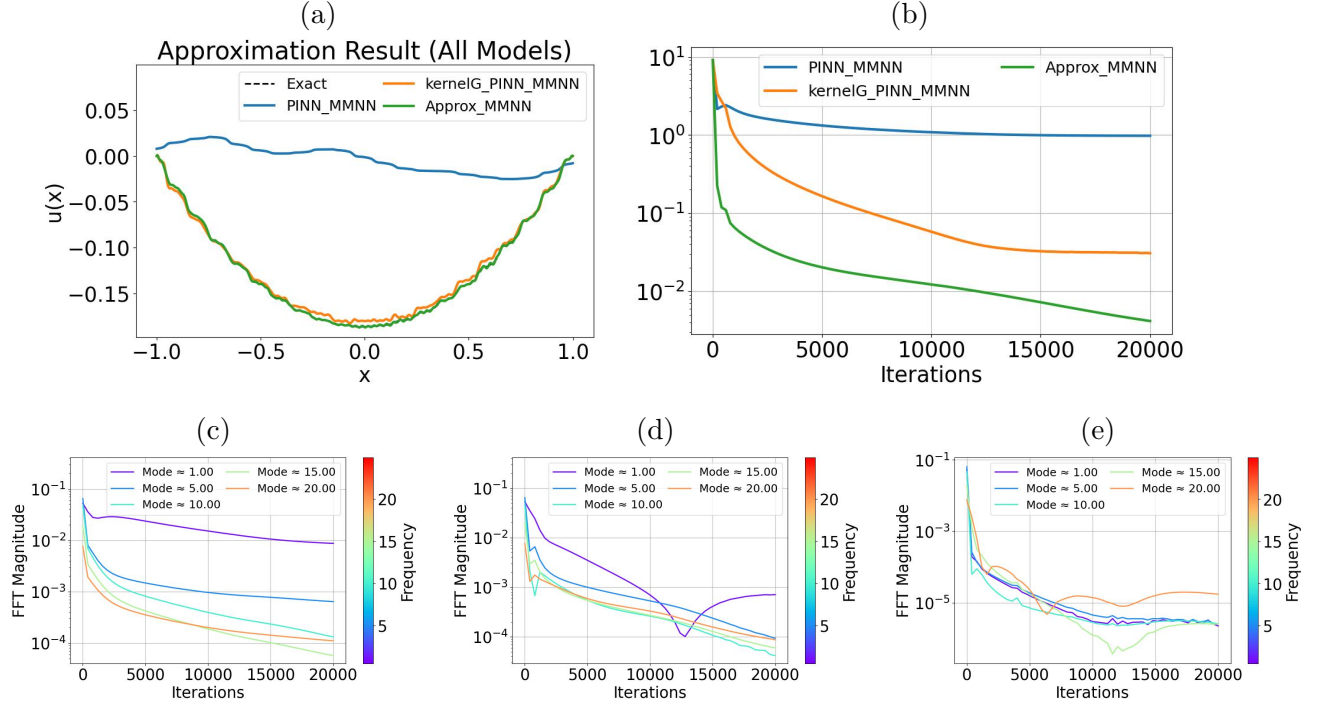


Figure 7: Example 6(b): (a) Exact solution and numerical results using MMNN; (b) L^2 relative error history; Errors in selected modes for PINN (c), preconditioned PINN (d), and approximation (e).

Dirichlet boundary conditions, and the source function f is chosen such that the exact solution is

$$\begin{aligned}
 u_3(x) &= 1.0 \cdot \phi(x; c^{(1)}, 0.8) \\
 &\quad + 0.7 \cdot \phi(x; c^{(2)}, 0.2) \\
 &\quad + 0.5 \cdot \phi(x; c^{(3)}, 0.1) \\
 &\quad + 0.3 \cdot \phi(x; c^{(4)}, 0.1),
 \end{aligned}$$

where

$$c^{(1)} = (0.0, 0.0), \quad c^{(2)} = (0.6, 0.6), \quad c^{(3)} = (-0.5, 0.3), \quad c^{(4)} = (0.2, -0.7),$$

and ϕ is the smooth compactly supported bump function

$$\phi(x; c, s) = \begin{cases} \exp\left(-\frac{1}{1 - \frac{|x - c|^2}{s^2}}\right), & \text{if } |x - c| < s, \\ 0, & \text{otherwise.} \end{cases}$$

This creates a solution with four localized bumps of different amplitudes and scales, as shown in Fig. 8(a). The largest bump at the origin has scale 0.8, while the smallest bumps have scale 0.1, creating a multi-scale challenge. We use an MMNN architecture of width 200, rank 20 and depth 3, corresponding to 8,241 learnable parameters, and train with 10,000 collocation points.

Fig. 8(b) shows dramatic different decay in L^2 errors during training across the three tasks. When approximating the function directly, the MMNN achieves the fastest convergence, reaching a

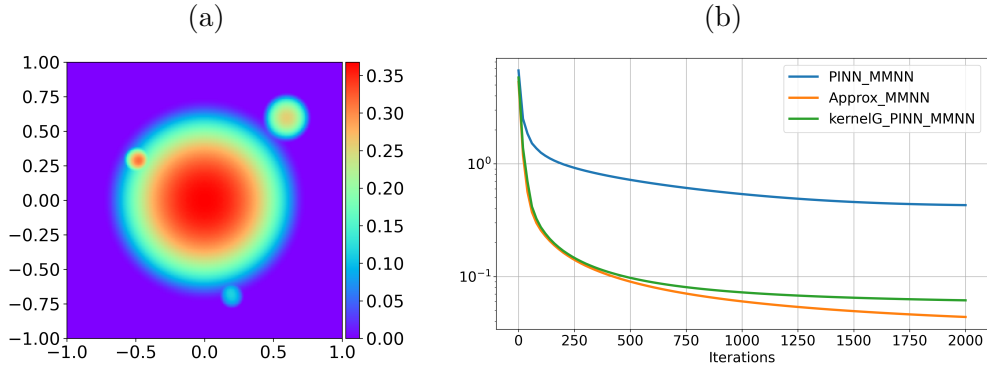


Figure 8: Example 7: (a) Exact solution; (b) Relative L^2 error during training for different models.

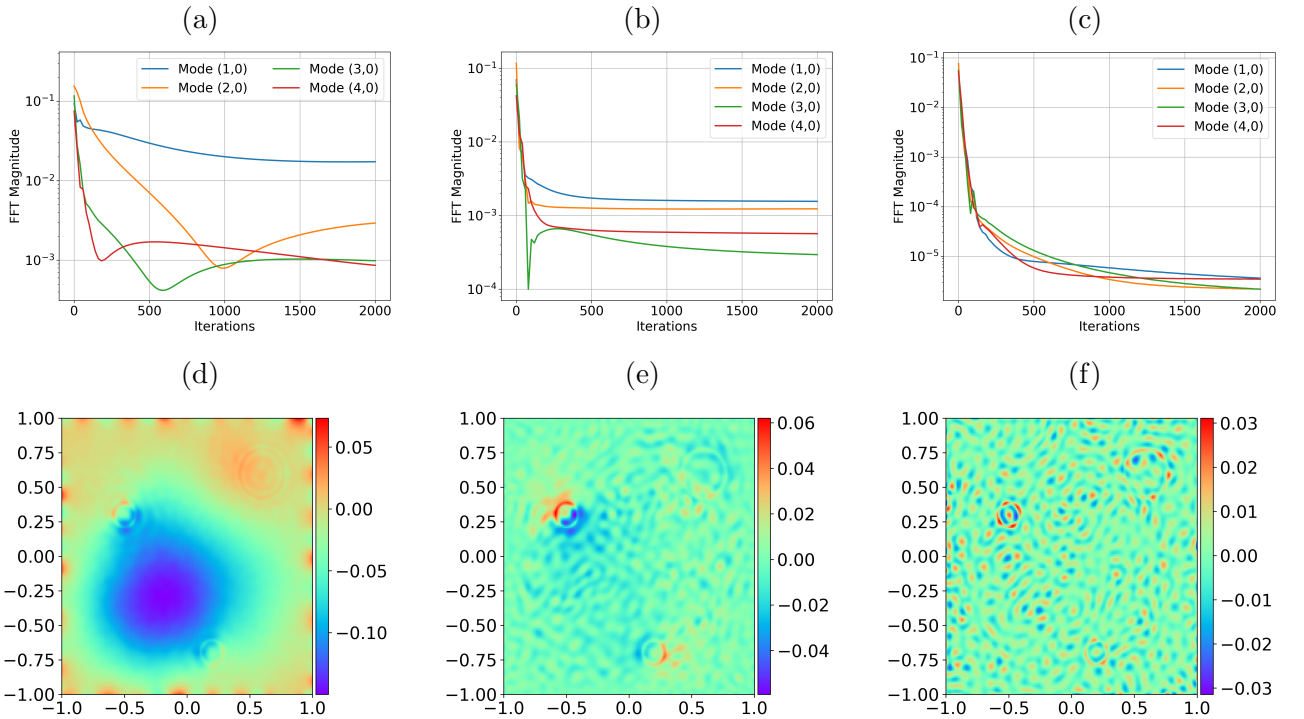


Figure 9: Example 7: Errors in selected modes for PINN (a), preconditioned PINN (b) and approximation (c); Spatial error distributions for PINN (d), preconditioned PINN (e) and approximation (f).

relative L^2 error of 4.38×10^{-2} in 2,000 epochs. In contrast, the standard PINN exhibits much slower convergence and plateaus at a larger error, with a relative L^2 error of 4.30×10^{-1} . The corresponding training times are 217 seconds for direct approximation, 259 seconds for the preconditioned PINN, and 256 seconds for the standard PINN. The preconditioned PINN has a significantly improved performance over the standard PINN, reducing the relative L^2 error to 6.15×10^{-2} , comparable to direct function approximation. These results and their underlying mechanism are revealed by the frequency bias shown in Figs. 9(a)–(c). Figs. 9(c) shows that FMMNN has little frequency bias and excellent convergence across all modes, which correlates well with its overall performance

in L^2 error. Due to the weak frequency bias of FMMNN as a representation, the involvement of differential operators in a standard PINN model will induce strong high frequency bias, as shown in Figs. 9(a), where the error in the lowest frequency mode decays very slowly. In contrast, the preconditioned PINN (Fig. 9(b)) exhibits much more uniform convergence across all modes, similar to the function approximation task, again verifying the effectiveness of our preconditioning strategy. These phenomena are further corroborated by the corresponding spatial error distributions shown in Figs. 9(d)–(f): the error for standard PINN mainly concentrates on the largest bump, whereas the preconditioned PINN and direct function approximation yield more randomized error distributions, i.e. in high frequency modes.

This example demonstrates that, when using well-designed NNs with good representation capability for high frequency modes and fine features (meaning weak frequency bias) to solve elliptic PDEs, proper preconditioning is crucial. Otherwise, it is difficult or costly to capture even a smooth solution using gradient-based training.

Example 8: In this example, we solve the Poisson equation $\Delta u = -f$ in the unit disk $\Omega = B(0, 1) \in \mathbb{R}^2$ with inhomogeneous Dirichlet boundary conditions. The exact solution is

$$u_4(x) = 0.3 \cdot \sin(4\pi x_1 + 2\pi x_1 x_2) + 0.05 \cdot \sin(12\pi x_2 + 4\pi x_1 x_2),$$

where $x = (x_1, x_2)$. We use an MMNN architecture of width 200, rank 40, and depth 3, corresponding to 16,281 learnable parameters, and train with 7,854 sample points.

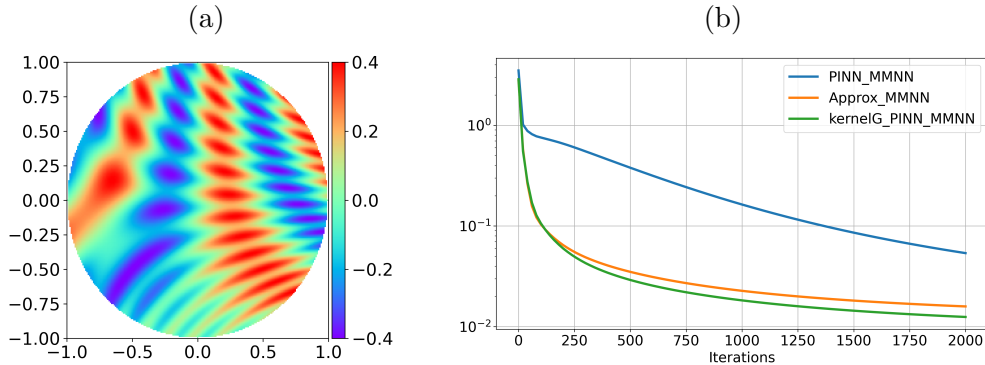


Figure 10: Example 8: (a) Exact solution; (b) Relative L^2 error during training for different models.

The results are presented in Fig. 10 and Fig. 11, which show behaviors and patterns similar to those in Example 7. The use of NN representation allows one to deal with domain geometry easily. The corresponding training times are 231 seconds for direct approximation, 253 seconds for the preconditioned PINN, and 250 seconds for the standard PINN.

Example 9: We consider a two-dimensional multiscale variable-coefficient problem as follows.

$$\begin{cases} \nabla \cdot (k(x)\nabla u) = -1 & \text{in } \Omega = (-1, 1)^2 \\ u = 0 & \text{on } \partial\Omega \end{cases},$$

where $x = (x_1, x_2)$ and the diffusion coefficient is defined by

$$k(x) = \frac{2 + A \sin\left(\frac{2\pi x_1}{\varepsilon}\right)}{2 + A \cos\left(\frac{2\pi x_2}{\varepsilon}\right)} + \frac{2 + A \sin\left(\frac{2\pi x_2}{\varepsilon}\right)}{2 + A \sin\left(\frac{2\pi x_1}{\varepsilon}\right)},$$

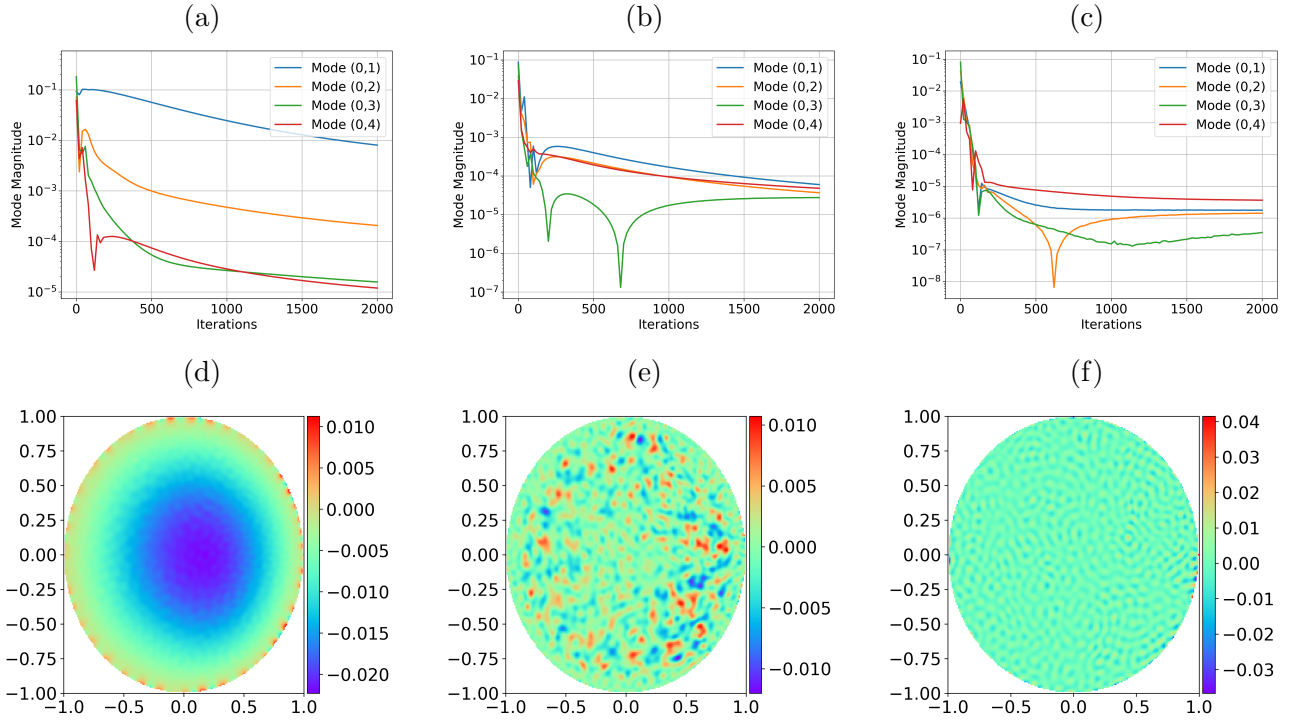


Figure 11: Example 8: Errors in selected modes for PINN (a), preconditioned PINN (b) and approximation (c); Spatial error distributions for PINN (d), preconditioned PINN (e) and approximation (f).

with $A = 1.8$ and $\varepsilon = 0.3$. This choice creates a diffusion coefficient with rapid oscillations in both directions. The PDE solution (Fig.12 (a)) exhibits a smooth macroscopic profile modulated by microscopic heterogeneity. We use an FMMNN architecture of width 200, rank 40, and depth 3, corresponding to 16,281 learnable parameters, and train with 10,000 sample points.

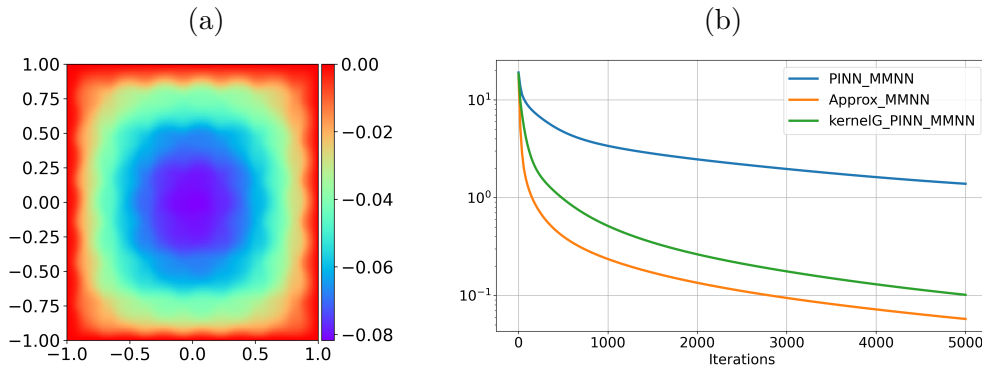


Figure 12: Example 9: (a) Exact solution; (b) Relative L^2 error during training for different models

This is a typical example of an equation with a multiscale feature in two dimensions. Without preconditioning, PINN fails to capture the solution, maintaining a relative L^2 error of 1.39, after 5,000 epochs. However, the preconditioned PINN achieves much better accuracy with relative L^2 error of 1.02×10^{-1} , although less accurate than the approximation with relative L^2 error of

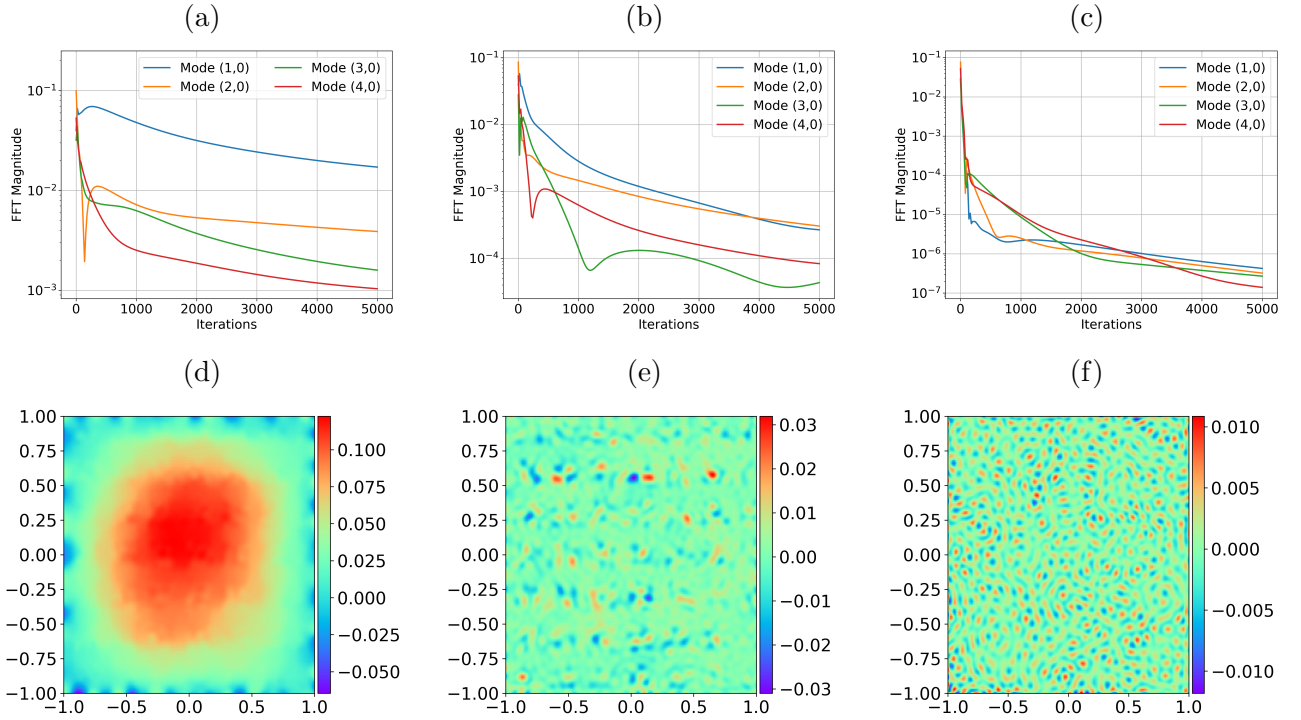


Figure 13: Example 9: Errors in selected modes for PINN (a), preconditioned PINN (b) and approximation (c); Spatial error distribution for PINN (d), preconditioned PINN (e) and approximation (f)

5.75×10^{-2} . While the free-space Green's function for the Laplace equation used is not the exact one for this variable-coefficient operator, the frequency bias caused by the differential operator is pretty well offset by the approximate preconditioning, which is shown both from the error mode dynamics and the error plot in Fig. 13. This example demonstrates that preconditioning remains effective even for challenging multiscale variable-coefficient problems where the preconditioner is only approximate.

Example 10: We solve the Poisson equation $\Delta u = -f$ in a unit ball $\Omega = B(0, 1) \subset \mathbb{R}^3$ with homogeneous Dirichlet boundary conditions, and the source function f is chosen such that the exact solution is

$$\begin{aligned}
 u(x) = & 1.0 \cdot \phi(x; c^{(1)}, 0.8) \\
 & + 0.7 \cdot \phi(x; c^{(2)}, 0.4) \\
 & + 0.5 \cdot \phi(x; c^{(3)}, 0.3),
 \end{aligned}$$

where

$$c^{(1)} = (0.0, 0.0, 0.0), \quad c^{(2)} = (0.5, 0.5, 0.1), \quad c^{(3)} = (-0.4, 0.3, -0.1),$$

and ϕ is the smooth compactly supported bump function

$$\phi(x; c, s) = \begin{cases} \exp\left(-\frac{1}{1 - \frac{|x - c|^2}{s^2}}\right), & \text{if } |x - c| < s, \\ 0, & \text{otherwise.} \end{cases}$$

We use an MMNN architecture of width 200, rank 40, and depth 3, corresponding to 16,281 learnable parameters, and train with 65,450 sample points.

In the three-dimensional setting, the frequency bias is analyzed using a spectral decomposition based on spherical Bessel functions and spherical harmonics. We consider basis functions of the form

$$j_\ell(z_{\ell n}r) Y_{\ell m}(\theta, \varphi),$$

which form an orthogonal system in the unit ball. Here j_ℓ denotes the spherical Bessel function of order ℓ , $Y_{\ell m}$ is the spherical harmonic of degree ℓ and order m , $r = |x|$, and $z_{\ell n}$ is the n -th positive zero of j_ℓ . Each mode is indexed by a triplet (ℓ, m, n) , where ℓ controls the angular frequency, m specifies the angular orientation, and n determines the radial frequency. To investigate frequency-dependent learning behavior, we track a selected set of modes (ℓ, m, n) to quantify how different spatial frequencies are learned. In addition, we visualize the spatial error on the cross-section $z = 0$. The results are presented in Fig. 14 and Fig. 15, which show behaviors and patterns similar to those in the two-dimensional case. The mode dynamics and spatial error visualization verify that the frequency bias caused by the differential operator is substantially mitigated by the approximate preconditioning in the three-dimensional setting.

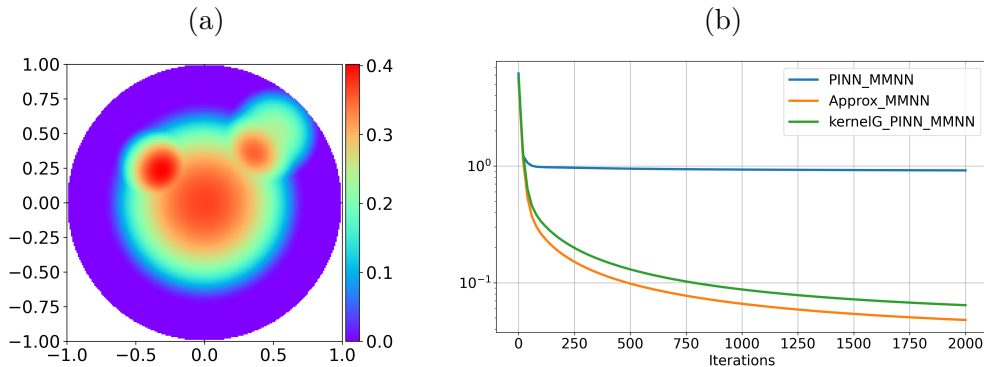


Figure 14: Example 10: (a) Cross-section of the exact solution at $z = 0$; (b) Relative L^2 error during training for different models.

6 Conclusion

In this work, we investigated the competition and balance between the spectral biases in NN representation and the differential operator when NNs are trained to solve elliptic PDEs. While strong low frequency bias of two-layer NNs will dominate differential operators as shown in [HLZZ25], the situation can be quite different for multilayer NNs, which can have powerful representation capability and weak frequency bias when properly designed. In this work, it is shown that the inherent high frequency bias of a differential operator may dominate the overall formulation, which makes training inefficient even for smooth solutions.

To address this issue, we propose an operator-aware preconditioning strategy that explicitly offsets the frequency bias of the differential operator and improves both efficiency and accuracy of the training process significantly. Extensive numerical experiments demonstrate the effectiveness of our strategy.

A key take-home message from this study is that understanding spectral behaviors, which are strongly correlated with the efficiency and accuracy of NN representation and its training

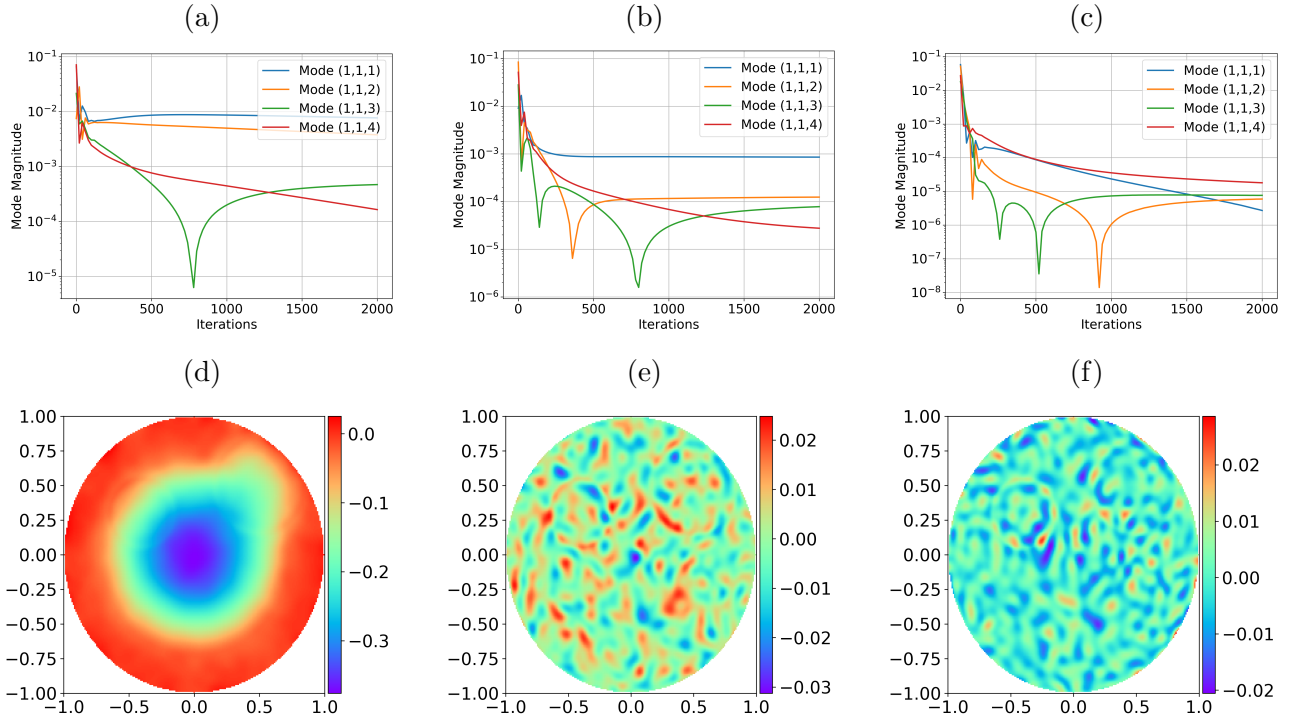


Figure 15: Example 10: Errors in selected modes for PINN (a), preconditioned PINN (b) and approximation (c); Spatial error distributions for PINN (d), preconditioned PINN (e) and approximation (f).

process, is essential in practice. The operator-aware perspective proposed in this work suggests an effective problem-dependent approach, which also leads to interesting questions about other formulations, such as the deep Ritz method and other variational or residual-based neural solvers. Furthermore, in more complicated problems, such as operator learning, multiple competing loss terms, such as interior residuals, boundary errors, and operator evaluations, may exhibit distinct spectral behaviors, leading to complex training dynamics. The design of effective preconditioning strategies that can achieve an overall spectral balance will be essential.

Acknowledgments

Hongkai Zhao is partially supported by the National Science Foundation through grant DMS-2309551. Yimin Zhong is partially supported by the National Science Foundation through grant DMS-2309530. Roy Y. He is partially supported by NSFC grant 12501594, PROCORE-France/Hong Kong Joint Research Scheme by the RGC of Hong Kong and the Consulate General of France in Hong Kong (F-CityU101/24), StUp - CityU 7200779 from City University of Hong Kong, and the Hong Kong Research Grant Council ECS grant 21309625.

References

- [ATSK24] Sokratis J Anagnostopoulos, Juan Diego Toscano, Nikolaos Stergiopoulos, and George Em Karniadakis. Residual-based attention in physics-informed neural net-

- works. *Computer Methods in Applied Mechanics and Engineering*, 421:116805, 2024.
- [Bar02] Andrew R Barron. Universal approximation bounds for superpositions of a sigmoidal function. *IEEE Transactions on Information theory*, 39(3):930–945, 2002.
- [BD20] David GT Barrett and Benoit Dherin. Implicit gradient regularization. *arXiv preprint arXiv:2009.11162*, 2020.
- [BGG⁺20] Ronen Basri, Meirav Galun, Amnon Geifman, David Jacobs, Yoni Kasten, and Shira Kritchman. Frequency bias in neural networks for input of non-uniform density. In *International conference on machine learning*, pages 685–694. PMLR, 2020.
- [CFW⁺21] Yuan Cao, Zhiying Fang, Yue Wu, Ding-Xuan Zhou, and Quanquan Gu. Towards understanding the spectral bias of deep learning. In *30th International Joint Conference on Artificial Intelligence (IJCAI 2021)*, pages 2205–2211. International Joint Conferences on Artificial Intelligence, 2021.
- [CGP06] Shivkumar Chandrasekaran, Ming Gu, and Timothy Pals. A fast and stable solver for hierarchically semi-separable (hss) representations of structured matrices. *SIAM Journal on Matrix Analysis and Applications*, 28(3):817–839, 2006.
- [Cyb89] George Cybenko. Approximations by superpositions of a sigmoidal function. *Mathematics of Control, Signals and Systems*, 2:183–192, 1989.
- [DHP21] Ronald DeVore, Boris Hanin, and Guergana Petrova. Neural network approximation. *Acta Numerica*, 30:327–444, 2021.
- [DJL⁺22] Chenguang Duan, Yuling Jiao, Yanming Lai, Dingwei Li, Jerry Zhijian Yang, et al. Convergence rate analysis for deep ritz method. *Communications in Computational Physics*, 31(4):1020–1048, 2022.
- [DRBmDB23] Tim De Ryck, Florent Bonnet, Siddhartha Mishra, and Emmanuel de Bézenac. An operator preconditioning perspective on training in physics-informed machine learning. *arXiv preprint arXiv:2310.05801*, 2023.
- [DRMM24] Tim De Ryck, Siddhartha Mishra, and Roberto Molinaro. wpinns: Weak physics informed neural networks for approximating entropy solutions of hyperbolic conservation laws. *SIAM Journal on Numerical Analysis*, 62(2):811–841, 2024.
- [ES16] Ronen Eldan and Ohad Shamir. The power of depth for feedforward neural networks. In *29th Annual Conference on Learning Theory (COLT)*, volume 49 of *Proceedings of Machine Learning Research*, pages 907–940. PMLR, 2016.
- [EY18] Weinan E and Bing Yu. The deep ritz method: A deep learning-based numerical algorithm for solving variational problems. *Communications in Mathematics and Statistics*, 6(1):1–12, 2018.
- [GR87] Leslie Greengard and Vladimir Rokhlin. A fast algorithm for particle simulations. *Journal of Computational Physics*, 73(2):325–348, 1987.
- [HLZZ25] Roy Y He, Ying Liang, Hongkai Zhao, and Yiming Zhon. What can one expect when solving pdes using shallow neural networks? *arXiv preprint arXiv:2510.27658*, 2025.

- [HSTX22] Qingguo Hong, Jonathan W Siegel, Qinyang Tan, and Jinchao Xu. On the activation function dependence of the spectral bias of neural networks. *arXiv preprint arXiv:2208.04924*, 2022.
- [JGH18] Arthur Jacot, Franck Gabriel, and Clément Hongler. Neural tangent kernel: Convergence and generalization in neural networks. *Advances in neural information processing systems*, 31, 2018.
- [KB15] Diederik P. Kingma and Jimmy Ba. Adam: A method for stochastic optimization. In Yoshua Bengio and Yann LeCun, editors, *3rd International Conference on Learning Representations, ICLR 2015, San Diego, CA, USA, May 7-9, 2015, Conference Track Proceedings*, 2015.
- [KL20] Patrick Kidger and Terry Lyons. Universal approximation with deep narrow networks. In *Proceedings of the 33rd Conference on Learning Theory (COLT)*, volume 125 of *Proceedings of Machine Learning Research*, pages 2306–2327. PMLR, 2020.
- [Kra14] Ilija Krasikov. Approximations for the bessel and airy functions with an explicit error term. *LMS Journal of Computation and Mathematics*, 17(1):209–225, 2014.
- [LBY22] Yiping Lu, Jose Blanchet, and Lexing Ying. Sobolev acceleration and statistical optimality for learning elliptic equations via gradient descent. *Advances in Neural Information Processing Systems*, 35:33233–33247, 2022.
- [LJP⁺21] Lu Lu, Pengzhan Jin, Guofei Pang, Zhongqiang Zhang, and George Em Karniadakis. Learning nonlinear operators via deeponet based on the universal approximation theorem of operators. *Nature machine intelligence*, 3(3):218–229, 2021.
- [LKA⁺20] Zongyi Li, Nikola Kovachki, Kamyar Azizzadenesheli, Burigede Liu, Kaushik Bhattacharya, Andrew Stuart, and Anima Anandkumar. Fourier neural operator for parametric partial differential equations. *arXiv preprint arXiv:2010.08895*, 2020.
- [LLW21] Yulong Lu, Jianfeng Lu, and Min Wang. A priori generalization analysis of the deep ritz method for solving high dimensional elliptic partial differential equations. In *Conference on learning theory*, pages 3196–3241. PMLR, 2021.
- [LPW⁺17] Zhou Lu, Hongming Pu, Feicheng Wang, Zhiqiang Hu, and Liwei Wang. The expressive power of neural networks: A view from the width. In *Advances in Neural Information Processing Systems (NeurIPS)*, 2017.
- [MM23] Siddhartha Mishra and Roberto Molinaro. Estimates on the generalization error of physics-informed neural networks for approximating pdes. *IMA Journal of Numerical Analysis*, 43(1):1–43, 2023.
- [MZ19] Johannes Müller and Marius Zeinhofer. Deep ritz revisited. *arXiv preprint arXiv:1912.03937*, 2019.
- [MZ22] Johannes Müller and Marius Zeinhofer. Error estimates for the deep ritz method with boundary penalty. In *Mathematical and Scientific Machine Learning*, pages 215–230. PMLR, 2022.

- [RBA⁺19] Nasim Rahaman, Aristide Baratin, Devansh Arpit, Felix Draxler, Min Lin, Fred A. Hamprecht, Yoshua Bengio, and Aaron Courville. On the spectral bias of neural networks. 2019.
- [RPK19] Maziar Raissi, Paris Perdikaris, and George E Karniadakis. Physics-informed neural networks: A deep learning framework for solving forward and inverse problems involving nonlinear partial differential equations. *Journal of Computational Physics*, 378:686–707, 2019.
- [RYK20] Maziar Raissi, Alireza Yazdani, and George Em Karniadakis. Hidden fluid mechanics: Learning velocity and pressure fields from flow visualizations. *Science*, 367(6481):1026–1030, 2020.
- [SDK20] Yeonjong Shin, Jerome Darbon, and George Em Karniadakis. On the convergence and generalization of physics informed neural networks. *arXiv e-prints*, pages arXiv–2004, 2020.
- [SJHH21] Hwijae Son, Jin Woo Jang, Woo Jin Han, and Hyung Ju Hwang. Sobolev training for physics informed neural networks. *arXiv preprint arXiv:2101.08932*, 2021.
- [SYZ22] Zuowei Shen, Haizhao Yang, and Shijun Zhang. Deep network approximation: Achieving arbitrary accuracy with fixed number of neurons. *Journal of Machine Learning Research*, 23(276):1–60, 2022.
- [Sze39] Gabor Szeg. *Orthogonal polynomials*, volume 23. American Mathematical Soc., 1939.
- [TSM⁺20] Matthew Tancik, Pratul Srinivasan, Ben Mildenhall, Sara Fridovich-Keil, Nithin Raghavan, Utkarsh Singhal, Ravi Ramamoorthi, Jonathan Barron, and Ren Ng. Fourier features let networks learn high frequency functions in low dimensional domains. *Advances in neural information processing systems*, 33:7537–7547, 2020.
- [TYZZ25] Tao Tang, Jiang Yang, Yuxiang Zhao, and Quanhui Zhu. Structured first-layer initialization pre-training techniques to accelerate training process based on rank. *arXiv preprint arXiv:2507.11962*, 2025.
- [WWP21] Sifan Wang, Hanwen Wang, and Paris Perdikaris. On the eigenvector bias of fourier feature networks: From regression to solving multi-scale pdes with physics-informed neural networks. *Computer Methods in Applied Mechanics and Engineering*, 384:113938, 2021.
- [YBZ04] Lexing Ying, George Biros, and Denis Zorin. A kernel-independent adaptive fast multipole algorithm in two and three dimensions. *Journal of Computational Physics*, 196(2):591–626, 2004.
- [ZBYZ20] Yaohua Zang, Gang Bao, Xiaojing Ye, and Haomin Zhou. Weak adversarial networks for high-dimensional partial differential equations. *Journal of Computational Physics*, 411:109409, 2020.
- [ZZZZ25a] Shijun Zhang, Hongkai Zhao, Yimin Zhong, and Haomin Zhou. Fourier multi-component and multi-layer neural networks: Unlocking high-frequency potential. *arXiv preprint arXiv:2502.18959*, 2025.

- [ZZZZ25b] Shijun Zhang, Hongkai Zhao, Yimin Zhong, and Haomin Zhou. Structured and balanced multicomponent and multilayer neural networks. *SIAM Journal on Scientific Computing*, 47(5):C1059–C1090, 2025.
- [ZZZZ25c] Shijun Zhang, Hongkai Zhao, Yimin Zhong, and Haomin Zhou. Why shallow networks struggle to approximate and learn high frequencies. *Information and Inference: A Journal of the IMA*, 14(3):iaaf022, 2025.